Efficient GNSS Signal Acquisition Method for GNSS/GNSS-R Software-Defined Receivers

Shamil Samigulin

A THESIS SUBMITTED TO THE FACULTY OF GRADUATE STUDIES IN PARTIAL FULFILLMENT OF THE REQUIREMENTS FOR THE DEGREE OF MASTER OF SCIENCE

GRADUATE PROGRAM IN EARTH AND SPACE SCIENCE

YORK UNIVERSITY

TORONTO, ONTARIO

MAY 2023

Abstract

This thesis presents a novel acquisition algorithm for Global Navigation Satellite Systems (GNSS) that can be efficiently implemented on small digital devices such as software defined radios (SDRs) field programmable gate arrays (FPGAs). The algorithm is designed to improve the performance of GNSS signal acquisition for applications in GNSS reflectometry (GNSS-R), a remote sensing technique that uses GNSS signals as a source of information. Using pre-acquisition processing and partial correlation, the proposed algorithm reduces the computational complexity of conventional GNSS acquisition methods by ~ 27 times, making it suitable for such low-cost devices. The thesis begins by introducing the GNSS technology and its spectrum, followed by a review of existing acquisition algorithms and their application in GNSS reflectometry. The novel acquisition strategy is developed, and its performance discussed, along with opportunities for future work.

Acknowledgments

I am grateful to my co-supervisors, Professor Regina Lee and Professor Sunil Bisnath, for their patience and faith in me. Their invaluable advice has not only helped me in my research but also in life. I am sure that their dedication has laid the foundation for my scientific eagerness. I would also like to extend my heartfelt thanks to my parents for their constant encouragement throughout my studies. Thank you, Mom, and Dad.

Table of Contents

List of Tables

List of Figures

List of Acronyms

ADC	Analog to digital converter
AGC	Automatic gain control
ASIC	Application specific integrated circuit
BOC	Binary offset carrier
C/A	Coarse-acquisition code
CDMA	Code division multiple access
DBZP	Double block zero padding
DBZPTI	Double block zero padding transition insensitive
DDM	Doppler-delay map
DSSS	Direct sequence spread spectrum
ESA	European Space Agency
FDMA	Frequency division multiple access
FFT	Fast Fourier transform
FIR	Finite impulse response
FPGA	Field Programmable Gate Arrays
GNSS	Global Navigation Satellite System
GNSS-R	Global Navigation Satellite System Reflectometry
GPS	Global Positioning System
L-Band	Aeronautical band
LCHP	Left hand circular polarization
LFSR	Linear feedback shift register
PCPS	Parallel code phase search
PRN	Pseudorandom bit sequence
RCHP	Right hand circular polarization
SDR	Software-defined radios
SMC	Soil moisture content

Chapter 1: Introduction

This chapter provides an overview global navigation satellite (GNSS) technology and its applications. It discusses the problem of conventional GNSS acquisition algorithms being computationally complex and limited for use on small digital devices. An objective and outline of the thesis are presented.

1.1 Global Navigation Satellite System and Reflectometry

GNSS constellations of satellites broadcasts timing and orbital information around the globe. GNSS receivers access the constellation to provide users with accurate timing and positioning information (Kaplan et al. 2017). Initially there were two constellations: the Global Positioning System (GPS), developed by the U.S. and GLONASS, developed by the Soviet Union. This group has expanded to include Galileo, developed by European Union (EU), and BeiDou, developed by China, and several regional systems.

GNSS is currently used for various civil and non-civil applications, such as aviation, rail, maritime, land surveying, precise orbit determination, navigation, finance, telecommunication, and other space applications (Gleason et al., 2009; Gebre-Egziabher et al., 2009). Additionally, GNSS has been used as a tool for performing remote observations of Earth's atmospheric water vapor content (Männel et al., 2021; Antonoglou et al., 2022). More recently, GNSS signals have proven to be a powerful tool for opportunistic, multi-static remote sensing of diverse surface types around the globe (Paziewski et al., 2020). The reflection process of the Earth's surface modifies GNSS signals, allowing for the extraction of geophysical data and this application is called global navigation satellite system reflectometry (GNSS-R). GNSS can potentially be used for soil moisture content (SMC) retrieval (Masters et al., 2000; Jia et al., 2016). This application is a promising alternative to in-situ measurements or expensive radiometer methods, provided that a GNSS-R receiver exists with the functionality to acquire both direct and reflected signals and compute observables for reflectometry measurements.

The primary function of a GNSS-R receiver is to compute reflectometry observables typically called Delay Doppler Maps (DDM). The receiver uses a right-hand circular polarized (RHCP) antenna pointed towards zenith for reception of direct signals from GNSS satellites and a left hand circular polarized (LHCP) antenna pointed at nadir for reception of the reflected signals, an example of such setup can be found in Figure 1. An additional RHCP antenna or one additional dual-polarized antenna are also included pointing towards nadir direction as even weak RHCP reflected signals carry vital information for precise measurements for the estimation of soil moisture. The simultaneous software processing of DDMs is computationally intensive, making it more suitable as a post-processing task. To address this challenge, hardware accelerators such as Field Programmable Gate Arrays (FPGAs) are employed to significantly speed up the processing, enabling real-time capabilities (Marchan-Hernandez et al., 2008). For these components, the hardware consists of software reconfigurable digital hardware that provides the computational power necessary for a real-time GNSS-R receiver implementation, while providing flexibility of design and reconfigurability.

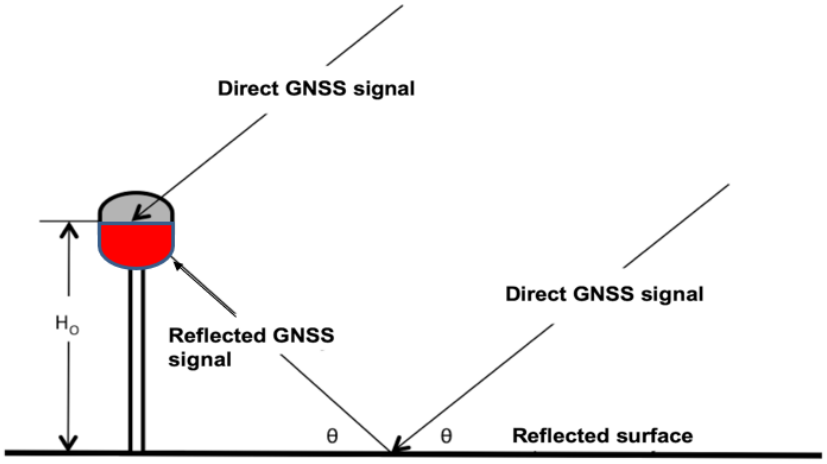

Figure 1. Stationary GNSS Reflectometry setup

GNSS signals are, in general, Direct Sequence Spread Spectrum (DSSS) systems (Hegarty 2003). Spreading codes with high autocorrelation and low cross correlation properties are used to spread the navigation message and serve as the basic tool for measuring the timing delay between the transmitting satellite and receiver. Each GNSS satellite within a constellation, with the exception of the satellites in the GLONASS constellation, is uniquely identified by a spreading sequence, making most GNSS systems Code Division Multiple Access (CDMA) systems (Zhuang et al., 1993).

All GNSS constellations operate on the shared astronautical band (L-band). The L-band, designated for satellite navigation thus, suffers low interference from external sources and penetrates the ionospheric and troposphere atmospheric layers. For GPS and Galileo, three frequencies exist on the band for satellite navigation: 1176.45 MHz (L5), 1227.60 MHz (L2), 1575.42 MHz (L1) (Hegarty 2012). The four modulations examined in this research are GPS L1 C/A-code, GPS L2C, GPS L5 I/Q, and Galileo E1-B. It is worth noting that Galileo E1-B shares the L1 band with GPS L1 C/A-Code. By examining multiple frequencies of the GPS constellation, a more precise reflectometry measurement can be performed over the surface due to varying penetration depth of each frequency. Including the Galileo constellation would increase the number of observable reflections, as the number of transmitters observed by the receiver is also increased. Overall, the GNSS spectrum is quite large and contains more modulations, Figure 2, shows all the available GNSS signals for civilian usage, and commercial usage, in addition to future signals.

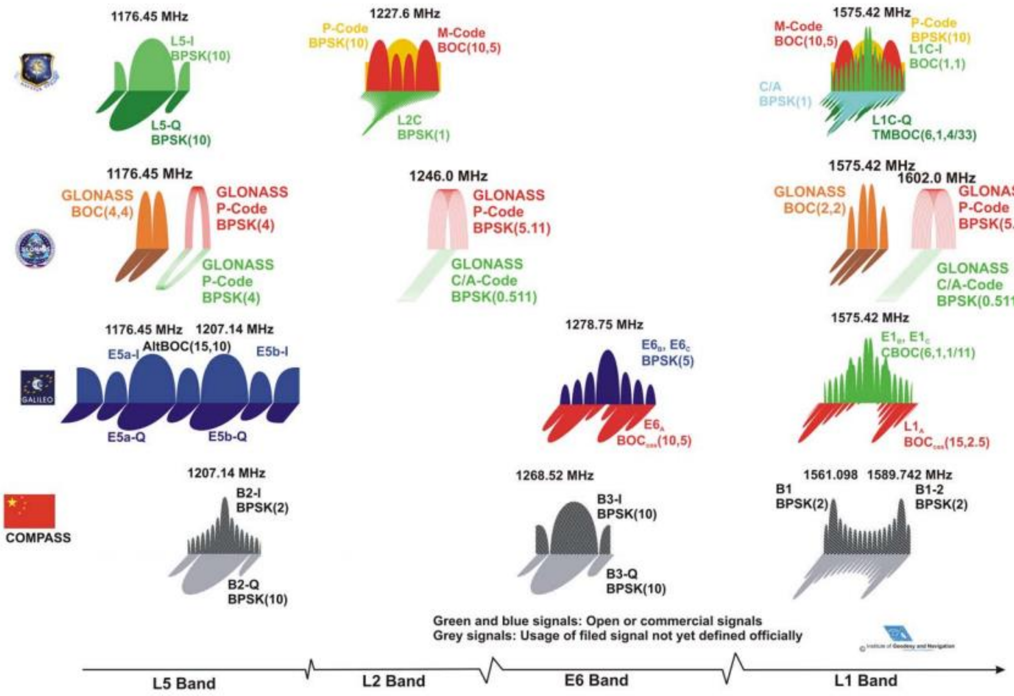

Figure 2. The GNSS Signal Spectrum, image credit to (Ávila Rodríguez, 2008)

1.2 Problem Statement

During acquisition, the GNSS receiver performs several tasks to receive a signal and compute reflectometry observables. As the weak signal cannot be directly accessed, a replica of the transmitted signal is generated to be correlated with the incoming signal (Kaplan et al. 2017). Conventional GNSS-R receivers use Fast Fourier Transforms (FFT) to generate the reflectometry observable DDM. However, this method requires large amounts of data and significant computation time, limiting its usefulness for real-time implementations (Borre et al. 2007). Therefore, it is crucial to analyze and examine the performance and data processing size requirements of the underlying software acquisition methodology, as well as optimize it to efficiently handle high sample rates. This presents a technical challenge that is addressed in this research. By overcoming this challenge, the benefits include improved efficiency and an increased number of observable reflections for a GNSS-R receiver.

1.3 Thesis Objectives

The goal of this research is to enhance the capabilities of a GNSS-R receiver by developing a new software-based approach for acquiring and processing a wide range of GNSS modulations. The proposed strategy, which supports multiple constellations and frequencies, is efficient in acquiring and computing DDMs from both direct and reflected signals, and reduces the need for large FFT transforms in real-time processing with FPGA hardware accelerators. The performance of this method is evaluated using MATLAB simulations, compared to the conventional parallel code phase search (PCPS) method, and analyzed in terms of execution time, successful detection rate, FFT size requirements, and the impact of signal strength on detection probability.

1.4 Thesis Outline

In Chapter 2, GPS L1 C/A, L2C L5 I/Q and Galileo E1 modulations are discussed, and their appropriate code and signal properties presented. Additionally, the concepts of GNSS front ends and GNSS-R receivers are reviewed. The conventional acquisition method is discussed, attention is drawn to the hardware chosen for the GNSS-R receiver implementation, and the challenge of implementing conventional acquisition methods for real-time processing is described.

In Chapter 3, the new efficient, Doppler and code delay estimation method is presented. The steps of the method are reviewed and shown. Also discussed is the theoretical detection performance of this proposed acquisition strategy. Finally, the software implementation of the strategy is presented and discussed.

Chapter 4 presents the details of the verification of the proposed method. A GSS9000 GNSS signal simulator and the simulator scenarios used for verification are explained. A detailed comparison is made between the results from the proposed method and the conventional method. The chapter ends with a presentation of weak signal acquisition performance for the proposed method. Finally, chapter 5 provides a summary and discussion of the results, and recommendations for future work.

Chapter 2: Software-defined Acquisition for GNSS-R Receiver

This chapter offers an introduction to GNSS and the different signal modulations it uses. It provides a detailed analysis of the civilian services of GPS L1 C/A, L2 CM, L5 I/Q, and Galileo E1-B, including their spectrum and code properties. Furthermore, the chapter discusses the remote sensing application of GNSS-R and how the proposed acquisition method is applied in this context.

2.1 General GNSS Signal Description

Satellite-based navigation utilizes DSSS, which is a spectrum modulation technique that significantly reduces overall signal interference and allows for multiple transmitters to share a singular frequency band. After dispreading or removal of the direct-sequence modulation in the receiver, the information can be restored. With DSSS, the information timing signals, and navigation data are modulated by a pseudorandom bit sequence (PRN) known as the code spreading sequence (Kaplan et al 2017). To protect the information from interference, each spreading-sequence bit (chip) has a much shorter duration than the original message bit. As a result, the modulation of the message bits scrambles and spreads out the information, and effectively encodes it within the bandwidth of the spreading sequence. The duration of the chip is inversely proportional to the bandwidth size: the shorter the duration, the larger the bandwidth, and the better the result against interference.

One practical and effective use of DSSS is CDMA, used by GPS, Galileo and BeiDou. GLONASS remains the sole frequency division multiple access system (FDMA) and is therefore not considered in this research. In essence, CDMA allows for a communication system to enable many users to share the same frequency band for transmission. For GPS, Galileo and BeiDou, each satellite in a constellation maintains a unique PRN code. Each of these codes have incredibly low cross-correlation and guaranteed high auto-correlation properties. These properties are desirable, as high autocorrelation allows for a receiver to correctly de-spread the received signal, and low-cross correlation guarantees the recovered information is interference free (Kaplan et al 2017). Shown in Figure 3 is the simplified receiver operation. Local replica of a PRN code and carrier frequency is correlated with incoming signal sample to derive the navigation and timing/ranging data. In Figure 3, the correlation operation on the received signal is performed to extract the underlying timing signals and navigation data. Each constellation and frequency band contains a unique version of a PRN code corresponding to an active, transmitting, in-orbit satellite. Consequently, each modulation also requires a different generation scheme which is described in the next section.

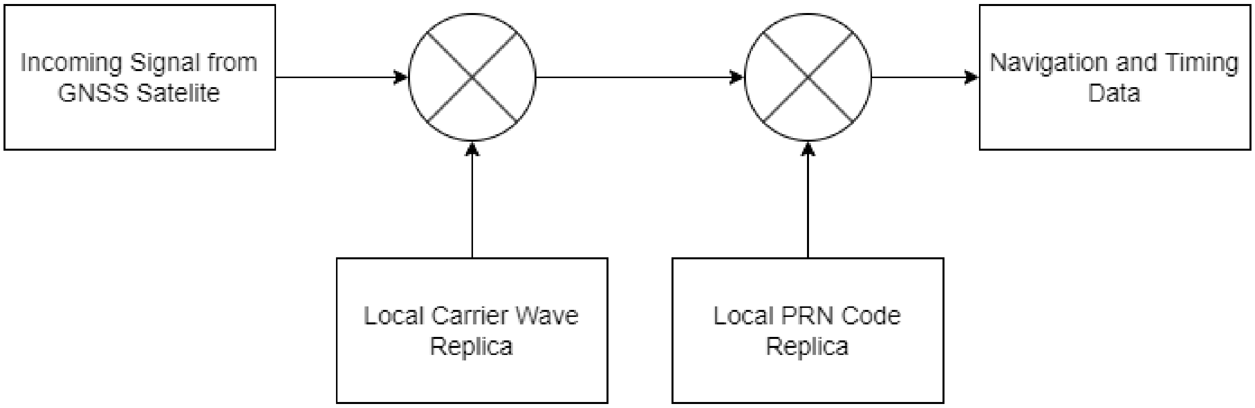

Figure 3. Simplified GNSS signal acquisition scheme

2.2 GPS L1, L2, L5 and Galileo E1-B Modulations

GPS transmits on 3 separate frequencies with numerous code modulations. The initial is transmitted on the L1 frequency and is called the Coarse-Acquisition code (C/A). L2C is the second civilian GPS modulation that has become available recently but has been in development since the late 1990's to facilitate weak signal users. Unlike the L1 C/A-code modulation, L2C is transmitted with a longer code duration for an improved reception for indoor users (Fontana et al 2001). The third signal is transmitted on the L5 band at much higher effective power than GPS L1 C/A and is called GPS L5 I/Q. The primary usage of the GPS L5 I/Q signal is for demanding aviation and safety of life applications (Spilker Jr et al, 2001). The next sections review the discussed codes' structures and generation methodologies.

2.2.1 L1 C/A-Code

Coarse-Acquisition code is a unique stream of bits that encodes the underlying navigation data. For the GPS, the C/A-code sequence is 1023 bits long, and is repeated roughly every millisecond, resulting in a frequency of 1.023 MHz. The unique sequences of the seeding bits are known as the Gold Codes. Figure 4 describes the generation of the C/A-code that is formed from the 'exclusive or' operator on the two linear-feedback shift (LFSR) registers G1 and G2 that synchronously generate two Gold Code sequences. Also shown are the feedback polynomials used to design the shift registers. The 32 unique codes are generated by selectively choosing taps from the G1 and G2 registers. In this context, the polynomial notation X^D represents a feedback term, with X denoting a binary bit and the exponent D representing the associated delay. From this point this notation will be used to describe the unique code generation schemes for each modulation. The summation of these terms results in a unique code sequence. This polynomial notation will be employed to describe the distinctive code generation scheme for each modulation technique. For further details, additional information can be found in the GPS ICD 200 document (NAVSTAR 2015). Consequently, each transmitting satellite in the GPS constellation is assigned a distinct Pseudo Random Noise (PRN) sequence generated from a Gold code, providing a unique identification for each satellite.

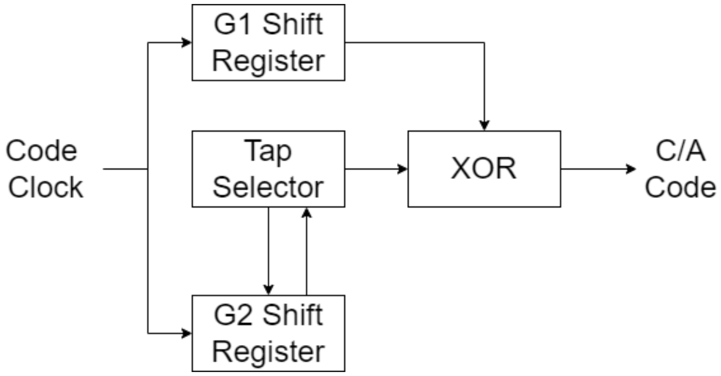

$$G1\ Shift\ Register\ Polynomial: 1 + X^3 + X^{10}$$

$$G2\ Shift\ Register\ Polynomial: 1 + X^2 + X^3 + X^6 + X^8 + X^9 + X^{10}$$

Figure 4. GPS L1 C/A-code generation scheme

$$s^k(n) = \sqrt{2P_c}(C^k(n)D^k(n)\cos(2\pi F_{IF}t)) + e(n) \qquad \text{Equation 1.}$$

Where P_c describes the transmitted power, C^k represent the C/A-code and $e(n)$ noise. The navigation data are represented by D^k and is XOR-ed with the C/A-code during transmission. The term F_{IF} represent the carrier frequency, t represents the period, and n is the index of the sample.

Equation 2 represents the cross-correlation of two C/A-code sequences. The terms C^i and C^k represent the C/A-code from 2 different satellites. The term j represents the lag, if the two C/A-codes differ the two sequences would not correlate with each other, thus correlation resolves to 0.

$$R_{ik}(j) = \sum_{l=0}^{1022} C^i(l)C^k(l+j) = 0 \text{ for all } j \qquad \text{Equation 2.}$$

Equation 3 represents auto-correlation that is the measure of similarity between a C/A-code sequence with itself and with lag. The C/A-code from satellite k, C^k, is maximally correlated when the lag is minimal (Borre et al 2007). Figure 5 shows the power spectrum density (PSD) of the modulation. The GPS L1 C/A-code contains a lobe with bandwidth of 2 MHz at the centre this location is where most of the useful navigation and timing signal data lies, since the code frequency is 1.023 MHz.

$$R_{kk}(j) = \sum_{l=0}^{1022} C^k(l)C^k(l+j) = 0 \text{ for all } j \geq 0 \qquad \text{Equation 3.}$$

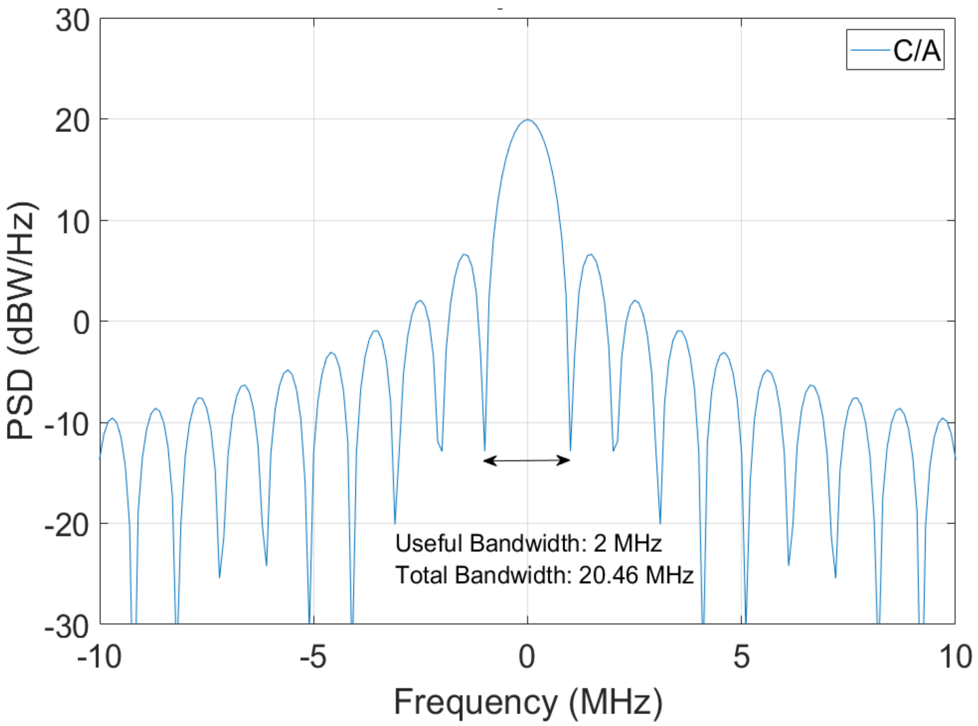

Figure 5. Power spectrum of normalized GPS L1 C/A-Code modulation.

2.2.2 L2C Modulation

L2C is a new civilian-use signal, composed of two ranging codes: one short 20 millisecond code (L2C) and a longer 1.5 second code (L2CL). The chipping rate of both codes is 511.5 KHz. Both code streams are time-multiplexed together to create the composite L2C code with frequency of 1.023 MHz (Navstar, 2015). As shown in Figure 6, the navigation message is modulated onto the shorter code L2C, which is then chip-by-chip, time-multiplexed with the longer L2CL code to formulate the composite GPS L2C signal.

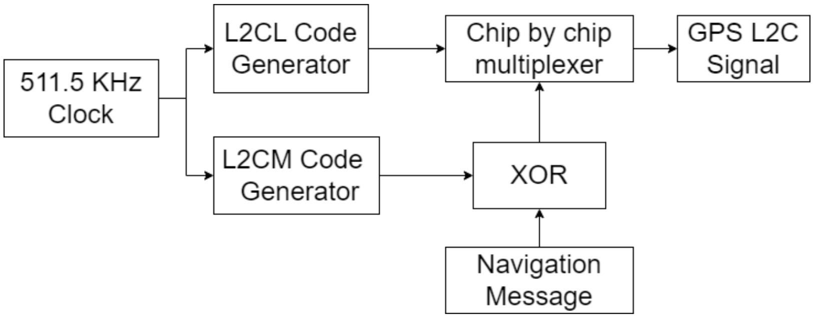

Figure 6. Generation of GPS L2C signal.

The GPS L2C signal code period is 20 milliseconds, requiring a longer integration time to be processed on the receiver. However, the benefit is increased reception under heavy canopy overgrowth and indoor environments. Unlike the L1 C/A-code that consists of Gold codes, the L2C code consists of what is known as the M-sequence. An M-sequence of code is a generalized maximal length polynomial that is of $2^n - 1$ in length, where n represents the maximum length defined as 27 bits for generation of the CM and CL codes. The resulting maximal polynomial is reset every 10,230 chips, thus resulting in a code sequence with a period of 20 milliseconds (Fontana et al 2001). Figure 7 depicts a block diagram of the 27-bit shift register employed for M-code generation. Both CM and CL codes employ the same shift register structure but with distinct initial states. In the figure, the red color signifies the feedback path, while the numbers within the boxes represent the delay. The updated information regarding M codes and the initial register states can be found in the GPS ICD 200 document (Navstar, 2015). The M-sequence of codes has the property of high autocorrelation at zero-lag and low cross correlation otherwise.

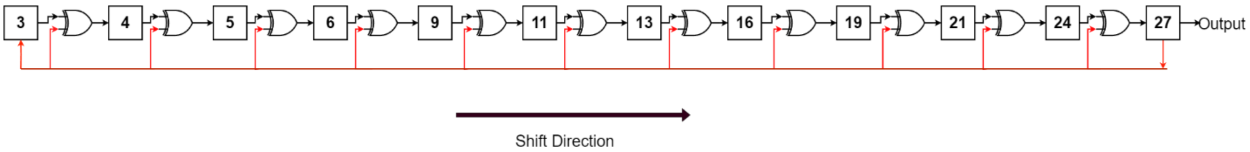

$$Polynomial: 1 + X^3 + X^4 + X^5 + X^6 + X^9 + X^{11} + X^{13} + X^{16} + X^{19} + X^{21} + X^{24} + X^{27}$$

Figure 7. Linear-feedback shift register block diagram for GPS L2CM and GPS L2CL code generation.

The total received signal is described in equation 5, where F_{L2} represents the L2 carrier frequency and P_c represents the received power, the ∪ is the union of $CM^k$and CL^{k} that represents the L2CM and L2CL time-multiplexing resulting in the composite L2C signal.

$$s^k{}_{L2C}(t) = \sqrt{2P_c}(CM^k(t) \cup \mathrm{CL}^{\mathrm{k}}(t)\ ) \oplus \mathrm{D}^{\mathrm{k}}(\mathrm{t}))\cos(2\pi F_{L2}t) \qquad \text{Equation 5.}$$

Equation 6, and 7 describe the cross and auto correlation properties of the L2C code. The term j represents the lag, if the two L2CM codes differ, the two sequences cannot correlate with each other, thus correlation resolves to 0. Otherwise, if both codes are aligned the result, resolves to 1. The power spectrum of GPS L2C is shown in Figure 8. The code frequency is 1.023 MHz, and the useful bandwidth component is centered around a 2 MHz bandwidth.

$$R_{ik}(j) = \sum_{l=0}^{10299} (CM^{ik}(l) \cup \mathrm{CL}^{\mathrm{ik}}(l))(CM^{ik}(l+j) \cup \mathrm{CL}^{\mathrm{ik}}(l+j)) \qquad \text{Equation 6.}$$

$$= 0\ for\ all\ j$$

$$R_{kk}(j) = \sum_{l=0}^{10299} (CM^{kk}(l) \cup \mathrm{CL}^{\mathrm{kk}}(l))(CM^{kk}(l+j) \cup \mathrm{CL}^{\mathrm{kk}}(l+j)) \qquad \text{Equation 7.}$$

$$= 0 \ for \ all \ j$$

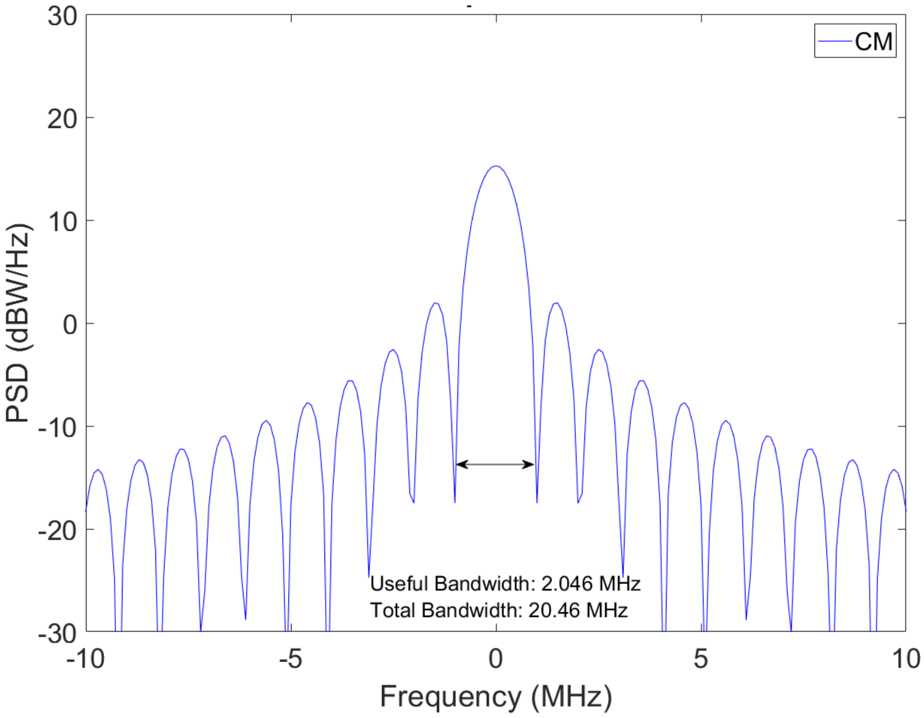

Figure 8. Power spectrum of normalized GPS L2C Modulation normalized.

2.2.3 L5 I/Q Code

The L5 I/Q modulation is intended to be transmitted at a frequency of 1176.60 MHz. It is transmitted at a higher power than the previous two modulations, in addition to having a more robust ranging code. Its primary usage is for safety-of-life, transportation, and other demanding applications, such as aviation. The L5 ranging codes are transmitted as the in-phase code L5-I; and the quadrature phase code L5-Q. Both codes are independent, but they are time synchronized. Therefore, each code is 10230 chips in length with a period of 1 millisecond (Spilker Jr et al 2001). The separate codes are generated using 3 separate linear-feedback shift registers. Figure 9 shows the 13-bit LFSR structure for generating the L5 I/Q ranging codes. The feedback polynomial used to generate the three registers are shown in the bottom of the figure. The XBI coder and XBQ generate the initial I code and Q code components. The XA coder then applies the "exclusive or" operator to generate the transmitted I and Q ranging codes. The XBI and XBQ coders have the same tap delays, so the difference is made from the initial states of each register.

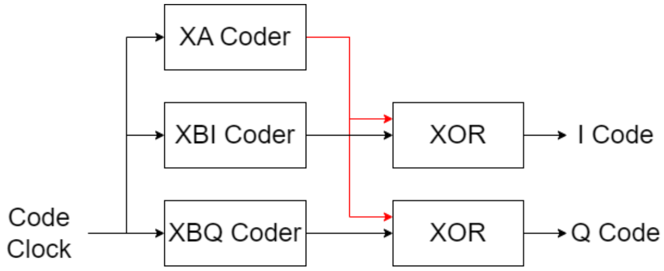

$$XB\ Polynomial = 1 + X + X^3 + X^4 + X^6 + X^7 + X^{12} + X^{13}$$

$$XA\ Polynomial = 1 + X^9 + X^{10} + X^{12} + X^{13}$$

Figure 9. Simplified linear feedback shift register structure for generation of GPS L5-I and GPS L5-Q codes the initial state of each register

The full GPS L5 specification including initial state of each LSFR register can be found in the GPS L5 Interface Control Document IS-GPS-705 (Navstar 2021). As in prior modulations, both the L5-I and L5-Q ranging codes experience high autocorrelation properties at zero lag and low cross correlation otherwise. Equation 9 describes the received L5-I signal, the pilot component L5-Q encoded by C_{XQ}^{k} is ignored and treated as noise $e(n)$, only the navigation data component is considered.

Equation 8 describes the received signal, where $\mathrm{P_C}$ is the received power, F_{L5} is the L5 carrier frequency, C_{XI}^{k} represents the code modulated by the navigation data, C_{XQ}^{k} represents the pilot code, D_{NH10}^{k} represents the 10 symbol Neuman-Hofmann code that encodes the underlying navigation data message, and NH_{20} represents the 20 symbol Neuman-Hofmann code that is the pilot component. As this thesis focuses on acquisition of the PRN ranging code, the Neuman-Hofmann codes represented by D_{NH10}^{k} and NH_{20} are out of scope. Post-ranging code acquisition, they are treated exactly like the navigation data message.

$$s^{k}{}_{L5I/Q}(t) = \sqrt{2P_c}((C_{XI}^{k}(t) \oplus D_{NH10}^{k}(t)) \cos(2\pi F_{L5}t) + (C_{XQ}^{k}(t) \oplus NH_{20}) \sin(2\pi F_{L5}t)) \qquad \text{Equation 8.}$$

Equation 9 describes the received L5-I signal, the pilot component L5-Q encoded by C_{XQ}^{k} is ignored and treated as noise $e(n)$, only the navigation data component is considered.

$$s^{k}{}_{L5I}(t) = \sqrt{2P}\left(C_{XI}^{k}(t) \oplus D_{NH10}^{k}(t)\right) \cos(2\pi F_{L5}t) + e(n) \qquad \text{Equation 9.}$$

Equation 10 describes the cross-correlation properties of the L5-I codes and Equation 11 describes the auto-correlation properties. The term j represents the lag, if the two L5-I codes differ the two sequences would not correlate with each other, thus correlation resolves to 0, otherwise if both codes are aligned the result resolves to 1. The power spectrum of the GPS L5 I/Q modulation is shown in Figure 9. The useful part of the bandwidth is shown, since the modulated code has a frequency of 10.23 MHz, most of the total bandwidth remains useful.

$$R_{ik}(j) = \sum_{l=0}^{10229} C_{XI}^{i}(l) C_{XI}^{k}(l+j) = 0 \text{ for all } j \qquad \text{Equation 10.}$$

$$R_{kk}(j) = \sum_{l=0}^{10229} C_{XI}^{k}(l) C_{XI}^{k}(l+j) = 0 \text{ for } j \geq 0 \qquad \text{Equation 11.}$$

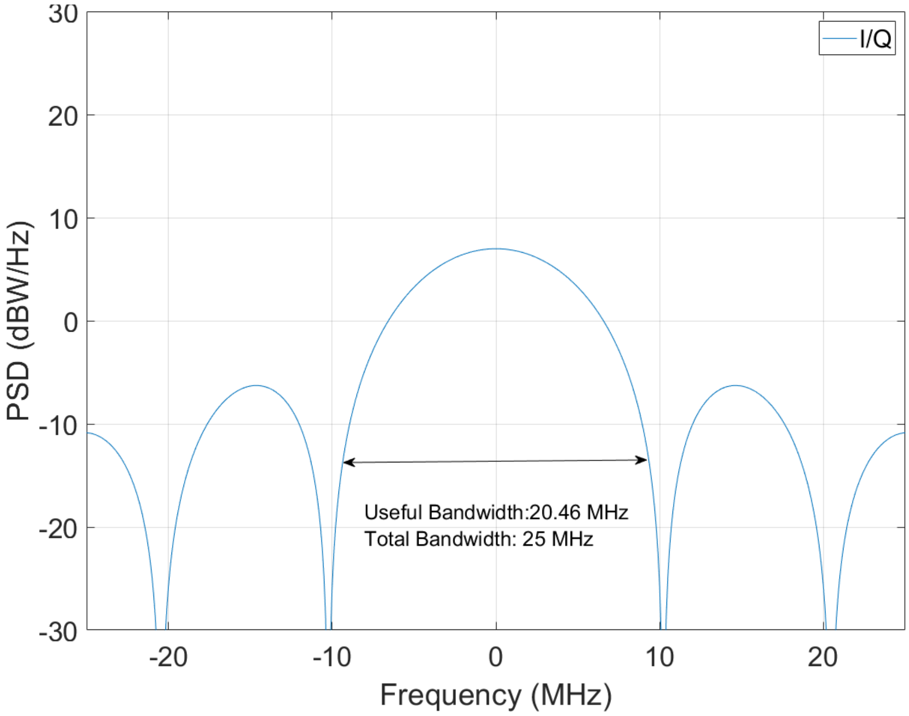

Figure 10. Power spectrum of normalized GPS L5 I/Q modulation.

2.2.4 Galileo E1 OS

The Galileo constellation is operated by the European Space Agency (ESA) for the EU. It was designed to be interoperable with the existing GPS constellation. It shares the L1, L2 and L5 bands with GPS. The E1 OS modulation, where OS stands for Open Service, is the civilian modulation provided by Galileo. It is transmitted on the L1 frequency, the signal is composed of three channels called A, B and C, where A is the restricted access signal (Borre et al 2007).

The total received signal is thus split into three components and shown in Equation 12. P_c is the received signal strength, the E1-B code is represented by C_{EB}, the E1-C code by C_{Ec} and, the E1-A code by C_{EA}, the F_{L1} represents the L1 carrier frequency. The E1-B channel is the data modulated signal that provides the navigation data, whilst the E1-C channel is the pilot component that contains a tiered code and provides no navigational data. Both the E1-B and C ranging codes are 4092 chips long and have a chipping rate of 1.023 MHz. The data component is modulated at a rate of 250 Hz, therefore providing the one code period per data symbol. The E1-C pilot channel contains a tiered code with a frequency of 25 Hz, and unlike the GPS constellation which utilizes the Gold sequence of codes that are generated by a tapped LSFR, Galileo utilizes Memory Codes. The advantage is that these codes are pre-generated and are read only from memory. The disadvantage remains an increase in memory requirements. For this work, only the E1-B channel is considered and is described by equation 13, where the pilot component E1-C and E1-A codes are treated as noise $e(n)$.

$$s^{k}{}_{E1B}(t) = \frac{\sqrt{2}}{3} P_c\big(C_{EB}(t) + C_{EC}(t)\big)\, cos(2\pi F_{L1} t) + \frac{1}{3} P_C(C_{EA}(t) + C_{EC}(t)C_{EA}(t)C_{EB}(t)) sin(2\pi F_{L1} t))$$ Equation 12.

$$s^{k}{}_{E1B}(t) = \frac{\sqrt{2}}{3} P_c\big(C_{EB}(t)\big) \cos(2\pi F_{L1} t) + e(n)$$ Equation 13.

Galileo, like GPS, utilizes the CDMA technique to provide an open service, and the generated ranging codes experience low cross correlation and high autocorrelation properties. One of the significant changes over GPS introduced by Galileo is the Binary Offset Carrier (BOC (M, N)) modulation. The BOC modulation offers two independent design parameters, the m or subcarrier frequency and n or spreading code rate. The two parameters provide the ability to concentrate the signal power with the specific part of the allocated band offering interoperability with existing modulations (Borre et al 2007). Figure 11 shows the BOC (M, N) signal that is created by modulating a sine carrier wave with the product of a PRN spreading code and a square wave subcarrier each represented by binary +/-1. Parameter M is the ratio between subcarrier and the reference frequency of 1.023 MHz and parameter N is the ratio between spreading code rate and the reference frequency.

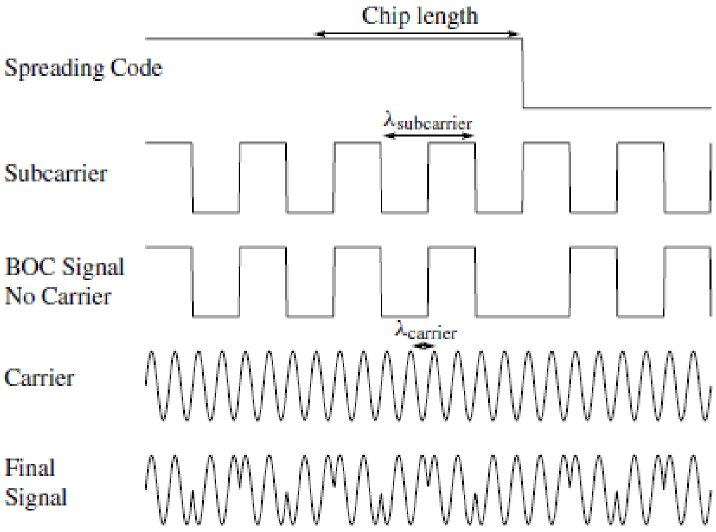

Figure 11. Generation of a BOC (M, N) signal (Borre 2007),

Equation 14 describes the cross-correlation properties of the E1-B code and Equation 15 describes the auto-correlation properties. The term j represents the lag, if the two E1-B codes differ the two sequences would not correlate with each other.

$$R_{ik}(j) = \sum_{l=0}^{4091} C_{EB}^{i}(l) C_{EB}^{k}(l+j) = 0 \text{ for all } j \qquad \text{Equation 14.}$$

$$R_{kk}(j) = \sum_{l=0}^{4091} C_{EB}^{k}(l) C_{EB}^{k}(l+j) = 0 \text{ for } j > 0 \qquad \text{Equation 15.}$$

The E1 OS system utilizes the BOC (1,1) modulation, which splits the classical BPSK spectrum into two symmetrical components. Figure 12 shows the power spectrum of the Galileo E1-B signal. The BOC modulation also creates a null at the centre of the spectrum to prevent interference with the GPS L1 C/A-code signal. This spreads 85% of the signal power within a 4 MHz bandwidth around the centre, allowing for the sharing of the L1 band between the GPS L1 C/A-code and E1 OS modulations.

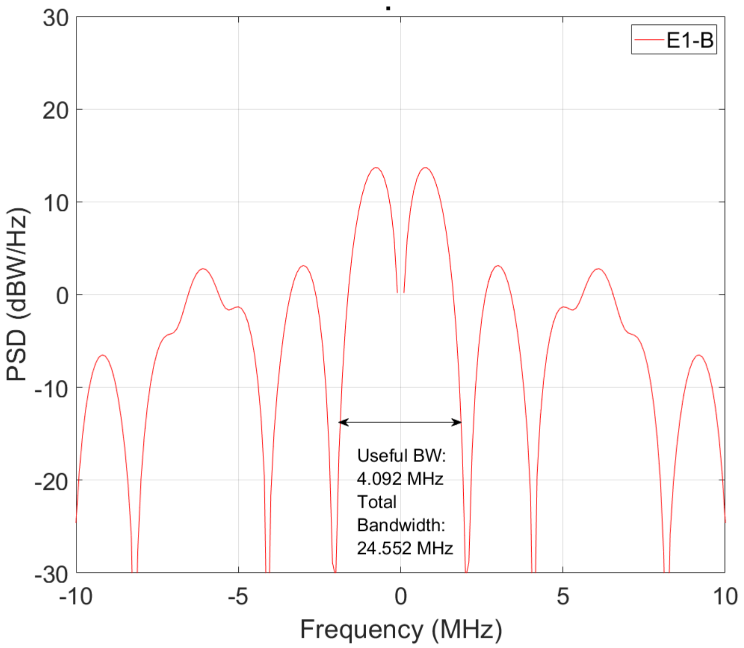

Figure 12. Normalized power spectrum of Galileo E1-B.

2.3 Software-Based GNSS Signal Acquisition

GNSS receiver designs use analog circuits for signal processing, which required the manufacturing and design of application specific circuits. These receivers are very fast, but are not reconfigurable post manufacturing, leading to obsolescence and the need for replacement. However, with the advancement of technology and the increase in processing power of personal computers, it has become possible to process these signals digitally. This concept is known as software-defined radio (SDR), which utilizes common digital signal processing hardware elements that can be reconfigured through software, offering greater flexibility and reconfigurability to the overall design (Mitola et al., 1993). Given that the transmitted GNSS carrier frequencies are in the mircowave portion of the spectrum, a GNSS SDR needs to utilize a GNSS front end (FE) for down conversion of the signal to a lower intermediate frequency (IF). The FE's primary responsibility is to provide a digital sample of the analog signal for software processing. An early GNSS SDR prototype was demonstrated by Krumvieda, K., et al (2001) with an IF software receiver capable of GPS L1 C/A-code acquisition. This concept was later expanded upon by Borre et al (2007) through the demonstration of a MATLAB-based GPS single channel software-defined receiver with the capability to acquire and track multiple satellites. As shown, the SDR concept has proven to be a reliable method for processing GNSS signals; however, it requires additional GNSS FE hardware to function. In the following subsections the concept of the GNSS FE is presented, and in later sections the common and the conventional software-defined acquisition methods are presented.

2.3.1 GNSS Front-End

A GNSS FE contains multiple components, and it can be seen as a wide-band analog to digital receiver. The GNSS signal is first sensed by the receiver’s antenna and is fed into the front-end section. The front-end is then responsible for filtering, down converting and quantization of the received analog signal.

Shown in Figure 13 is the functional description of a typical GNSS FE. The first component of the front-end radio frequency (RF) path is the band pass filter. A band pass filter is a frequency selective device that allows for certain frequency bands to pass, whilst attenuating others. Therefore, the filter can be characterized by two quantities: one known as insertion loss and bandwidth. The system noise parameter is determined by the insertion loss, which represents the attenuation of the incoming signal as it travels through the analog path from the antenna to the output. This value is typically presented in decibels (dB). Ideally this value should be 0 dB however in practice this value is minimized as much as possible (Kaplan et al 2017). The first filter goal is to provide a sharp transition between the desired and undesired frequency components. Following this stage, the signal is amplified by an in-line gain component to be then mixed.

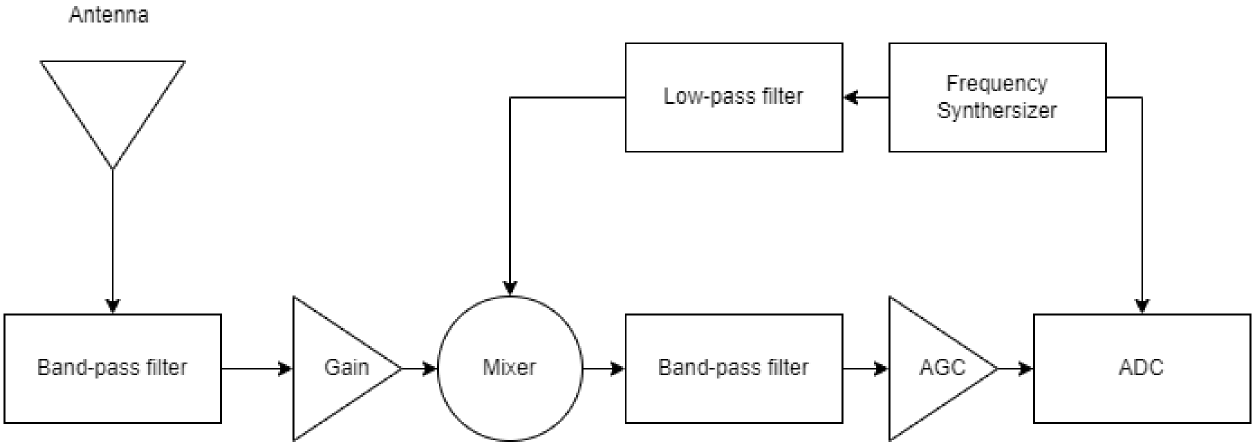

Figure 13. Typical GNSS RF-Front end block diagram, (after Borre et al. (2007))

The next stage of the RF path is the mixer/local oscillator, which converts the L1, L2 or L5 frequencies to a lowered frequency that can be digitally processed by a computer. The IF frequency is picked such that it can be sampled by an analog-to-digital converter. Typically, the oscillator would generate a frequency close to or near the desired frequency band. The result of mixing produces a signal that then consists of sum and difference of frequencies. Further filtering is necessary to obtain the desired IF frequency. For this purpose, a band-pass filter follows the mixing stage for which the band-pass filter bandwidth parameter is the desired IF. Following the filtering, the signal carrier frequency is now reduced to a frequency which can be converted to a digital representation.

The last stage of the RF path is the analog to digital converter (ADC). This stage determines how well the signal is preserved in the digital domain. This stage can be characterized by two properties: number of bits, and maximum sampling frequency. The main goal of the ADC is to quantize the analog signal into a binary representation. The choice of the number of bits for this task is crucial. Research has demonstrated that 1-bit quantization leads to a degradation of 2 dB (Bastide et al., 2003), whereas 2-bit or higher quantization reduces this degradation to 1 dB. Consequently, quantization beyond 2 bits yields diminishing returns, Therefore, in this thesis, quantization beyond 2 bits is not considered. The degradation penalty is dependent on whether there exists narrow-band interference. Ideally, the multi-bit sampling should be greater than 1-bit. For the purposes of multi-bit sampling the front-end also includes automatic gain control (AGC). The goal of the front-end is to utilize all the available bits in the ADC to achieve this, AGC is necessary. The AGC plays a crucial role in the front-end by amplifying weak signals and attenuating strong signals, working in conjunction with the ADC. This ensures that the signals received by the front-end are appropriately amplified and adjusted to maximize the utilization of the ADC's bit range. The specific gain characteristics and behavior of the AGC are typically designed and implemented as part of the front-end hardware. Finally, the sampling frequency considers the maximum sampled information bandwidth, and is determined by the desired intermediate frequency.

2.3.2 Serial Acquisition

The purpose of acquisition is to identify all “visible” satellites to the user. When a satellite is visible, the acquisition determines the coarse values of carrier frequency and code phase or time delay. The code phase parameter determines the timing alignment of the PRN codes in the current block of data such that a locally aligned replica is generated. The carrier varies due to the Doppler effect caused by the line-of-sight velocity of the satellite with respect to the receiver. From prior analysis in the literature, the generally accepted maximal frequency deviation is between -10 KHz and 10 KHz (Kaplan et al 2017). It is important to know this deviation to generate an exact carrier wave replica, inorder to remove the carrier from the signal.

A common method of acquiring a GNSS signal is called “Serial Search Acquisition” (Kaplan et al 2017). As the name implies, a serial search of the frequency and code phase is performed.

Figure 14 shows the block model of the algorithm provided: the incoming signal is multiplied by a locally PRN code replica, after which the signal is again multiplied by a local carrier wave replica. The resulting multiplication generates two components, the in-phase signal I, and the multiplication with 90° phase shifted version of the local carrier generates the quadrature signal Q. The signal generated at the satellite may not directly correspond to the demodulated I component due to the unknown phase during reception. Therefore, it is necessary to examine both the I and Q components of the signal to accurately analyze the received data. Both I and Q components are integrated over the duration of the code period, and the signal is squared and summed. In the ideal case, such as for GPS L1 C/A-code, the power in the in-phase part would be maximal and only noise would be in the quadrature part. If a pre-defined threshold is surpassed, the signal is therefore declared present.

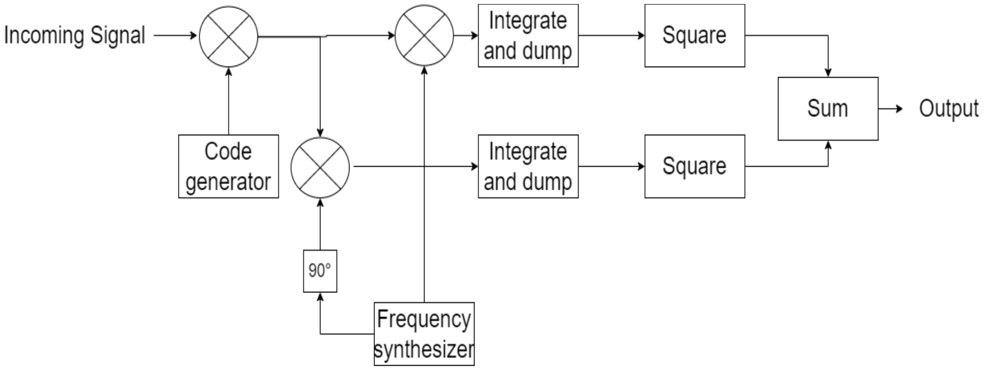

Figure 14. Serial Search Code Acquisition algorithm

Finally, this process is repeated for a variety of combinations of carrier frequency and code phase delay. The algorithm effectively performs two sweeps, a sweep for all possible carrier frequencies and a sweep for all possible code delays. As an example, in the case of the GPS L1 C/A-code, the maximal Doppler shift in any direction is 10 KHz. Therefore, if a Doppler frequency step search of 250 Hz is used and considering the length of 1023 chips of the PRN code, the total amount of repetitions can be totaled as: $1023 * (10{,}000\ \mathrm{Hz} * \frac{2}{250\ \mathrm{Hz}}) = 81{,}840$. Additionally, this search is repeated 32 times to sweep for all possible transmitting satellites. Therefore, these are a large number of combinations. The newer L5 I/Q and GPS L2C modulations contain much longer codes of 10,230, so the number of combinations is even larger. Therefore, while the implementation of the serial search is straightforward, the tremendous drawback of an exhaustive search routine makes it undesirable when considering the newly introduced modulations.

2.3.3 Parallel Acquisition

A more recent and faster search method called “Parallel Code Phase Search” (PCPS) is based on a method of performing circular correlation through FFT which reduces the number of computations (Tsui, J. 2005). The main idea behind this method is to parallelize the search space such that only a fraction of combinations is necessary to be computed by utilizing FFTs. Therefore, in this work, PCPS is considered as the conventional method. The mathematical description of the circular correlation operation using FFT is described in Oppenheim (1999). Figure 15 shows the block diagram of the PCPS method.

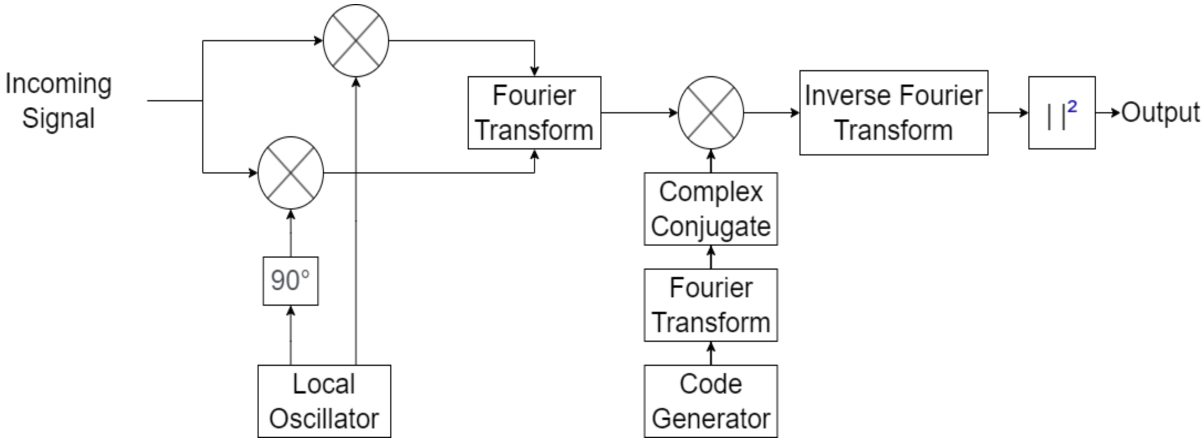

Figure 15. Parallel Code Phase Search algorithm

Initially, the signal is stripped of the carrier wave by multiplication with a local carrier replica and a 90-degree phase shifted replica, producing the I and Q signals, respectively. Thereafter, the I and Q components are combined to form a complex input to the Fourier transform function. The locally generated code replica is transformed into the frequency domain and the result is complex conjugated. The two resulting signals are multiplied in the frequency domain. Finally, a transformation back into the time domain by an inverse Fourier transform is performed. The resulting absolute value of the inverse transform is representative of the corresponding correlation between the input signal and the local code.

With the advantages of circular correlation, the total number of combinations and repetitions is reduced to the number of frequency steps required for the carrier sweep. As an example, the GPS L1 C/A-code's search step is 250 Hz and total search range is 10 KHz the total number of repetitions is defined as: $10\ \mathrm{KHz} \,/\, 250\ \mathrm{Hz} = 40$. In contrast, the computational efficiency remains to be affected by the Fourier transform blocks implementation and is proportional to the sampling frequency. Additionally, the PCPS method produces a more precise code delay estimation when compared to the serial search method, with PCPS the precision of code delay estimate depends on the sample size. e.g., if a GPS L1 C/A-code signal is sampled at a rate of 25 MHz, the resulting code delay can have 25,000 different values - effectively providing 25 samples per a single chip of the PRN sequence. In conclusion, given these enhancements, PCPS proves to be a solid choice as the conventional method over serial search.

2.4 Overview of GNSS Receivers for Reflectometry

GNSS was designed to provide position, navigation, and timing (PNT) information, and has additionally been used as signals of opportunity. The concept of GNSS-R involves using reflected GNSS signals to extract geophysical information from the changes experienced by these signals due to the reflection process on various types of Earth's surfaces (Rodriguez-Alvarez et al. 2010). The main benefits of GNSS-R. are: 1) GNSS is a well consolidated, calibrated and well supported constellation of transmitter satellites, and only receiver units need to be deployed serving as passive sensing instruments; and 2) GNSS has vast spatial coverage and frequent revisitation times due to having many transmitters available at the same time (Wu et al. 1997).

GNSS-R technology holds great potential and can be utilized by various user groups, including farmers, oceanographers, and similar professionals. Farmers can benefit from GNSS-R by using it for soil moisture content retrieval, providing them with valuable information for optimizing irrigation and crop management practices. Oceanographers can leverage GNSS-R for studying ocean surface parameters such as wave height, and wind speed. This data is crucial for understanding ocean dynamics, climate patterns, and coastal zone management. Similarly, scientists and researchers in related fields can also employ GNSS-R for studying various geophysical phenomena, such as land deformation, snow cover monitoring, and biomass estimation. The versatility of GNSS-R makes it a valuable tool for a wide range of applications, benefiting multiple user communities.

For example, applications are seen in ocean surface wind field retrieval (Clarizia et al 2008; Li et al 2014; Tsai et al 2021). Another successful application has been seen in sea ice detection

(Yan et al 2016). Further application of this concept extends to vegetation status measurements (Zribi et al 2019; Jia et al 2016), and as a tool for agriculture monitoring (Egido et al 2012). GNSS-R has been applied for both soil moisture content measurements (Chew et al 2016; Edokossi et al 2020; Camps et al 2020; Martín et al 2020), as well as estimation of snow depth (Qian et al 2016). Various airborne and satellite-based observational experiments have been conducted worldwide to actively promote GNSS-R's relevant applications. One of these experiments, the TDS-1 satellite launched by UK in 2014, is equipped with the SGR-ReSI GNSS-R technology demonstration (Unwin et al 2017). A more recent larger mission being conducted by National Aeronautics and Space Administration (NASA) with the launch of the CYGNSS constellation, launched in 2016 (Ruf et al 2017). In relation ESA is launching GERO-ISS as GNSS-R payload for the International Space Station (ISS) (Wickert et al 2013; Camps et al 2014).

Most of these space-based missions process the reflected GNSS signal on-board the satellite to generate DDMs as the main data product, which typically have a spatial resolution of 6-8 km. Although the provided data is valuable, the large spatial resolution proves to be limiting when determining precise localized geophysical measurements. For this reason, airborne GNSS-R experiments have been conducted that serve as an alternative method for gathering localized reflectometry data. An airborne example utilizing an Unmanned Aerial Vehicle (UAV), is presented in Troglia Gamba et al (2015) that demonstrated a GNSS-R receiver payload flown on a UAV for classifications of water content features of land. More recently, Imam et al (2020) demonstrated an application of UAV-based GNSS-R as a means of flood monitoring operations. GNSS-R receivers on-board commercial UAVs are constrained in the size, weight and are therefore restricted on computational power and must be carefully designed to meet the needs of reflectometry measurements. The next section reviews the existing compact GNSS-R receiver designs demonstrated by researchers.

2.4.1 Overview of Existing Airborne-based GNSS-R Receiver Designs

One of the main disadvantages of GNSS-R based receiver payloads is their heavy and bulky setup, which proves to be troublesome for UAV applications. To overcome this problem, some researchers designed and developed GNSS-R receivers, which are compatible with commercial UAVs, utilizing custom hardware components with software-based radio implementations. For example, Marchan-Hernandez et al (2008) designed the first of its kind FPGA-based GNSS-R receiver capable of processing two dimensional DDMs called PAU/GNSS-R. The receiver samples direct and reflected GNSS signals at a 1-bit quantization with a sampling rate of 5.745 MHz. The processing of the reflected DDMs is performed by a secondary FPGA, whilst direct signal acquisition is offloaded to a secondary standalone GPS receiver. The SDR on the FPGA generates DDMs via circularly correlating one millisecond samples of the GPS L1 C/A-code with the usage of an FFT. Each subsequent correlation is then integrated for a duration of one second to improve the subsequent signal-to-noise ratio. By performing real-time DDM computations, the overall amount of post-processing is reduced, and only immediately useful data are stored, reducing overall memory storage.

Other researchers proposed software receiver designs over single board computers to only store raw direct and reflected signal samples. For example, Esterhuizen (2006) presented a miniaturized receiver design utilizing two GPS L1 front ends and a x86 single board computer to store raw signal data for later post processing. While a more recent design such as the receiver presented in Troglia Gamba et al (2015) utilize an Odroid-X2 single board computer with two separate front ends that stores raw direct L1 and reflected L1, L2 and L5 signal samples for later post-processing. Most miniaturized GNSS-R receivers in the literature are composed of one or more GNSS front ends capturing direct signals from one zenith LHCP antenna and one nadir LHCP/RHCP antenna. Further examples are shown by Caparrini et al (2007) and Egido et al (2014). Due to the demanding processing requirement and large data size, the most opted route is to store and post-process raw signal samples on personalized computers. Although post processing is a convenient option, the data are not immediately useful and storing raw signal samples leads to greater storage requirements. The next section describes a new miniaturized multi-constellation and multi-frequency GNSS-R receiver design for real-time DDM generation, the chosen processing system and GNSS front-end that meet these requirements.

2.5 FPGA-based GNSS-R Receiver as a Soil Moisture Content Retrieval Payload for UAV

This research is part of a Canadian Space Agency (CSA) Flights and Fieldwork for the Advancement of Science and Technology (FAST) funding grant. The goal of the project is to demonstrate the application of GNSS-R by designing a GNSS-R receiver for a UAV payload as a technology demonstrator. One of the key requirements of the design is to include on-board processing of signal samples for DDM generation. The objective is to reduce the overall memory storage requirement of the payload, and to make the data immediately useful to the user after measurement. Another requirement is to observe multi-constellation and multi-frequency reflectometry data. By observing multiple GNSS constellations, the number of transmitters is effectively increased, providing more reflections. Additionally, by including multiple frequencies from the same constellation, greater precision in reflectometry measurements is achieved. This improves the accuracy of position and timing information and benefits the specular point estimations when performed in post-process. A feasibility study by Imam et al (2020) demonstrated this enhancement via simulation and noted an increase in specular points lines and improvement of water surface area estimations in post-process. Utilizing the GPS constellation alone provided an accuracy of 80%, while Galileo improved the accuracy to 90%.

To perform reflectometry measurements, the receiver requires three antennas: one facing zenith for direct signal sampling and two nadir antennas for sampling of reflected LHCP and

RHCP signals. Prior designs utilized two front-end to meet this design requirement; however, this design involves additional design work to synchronize the data streams coming from the two FE. To meet the requirement and to streamline the development process, the FE choice was narrowed down to the NTLab "NOMADA" NT-1065 (NTLAB 2020) which is shown in Figure 16. This FE embeds four synchronized receiving channels, each channel can be customized to cover the full L1, L2 or L5 band. Each channel feeds to the same embedded 2-bit analog-to-digital converter that generates a single concatenated 8-bit sample containing the 2-bit samples from the four individual channels. The sampling frequency is adjustable between 16 to 99 MHz, providing sufficient coverage for multi-constellation and multi-frequency reception. In this work, the FE was chosen to operate at the sampling rate F_S of 53 MHz and configured for sampling of GPS L1 C/A-code. L2C, L5 I/Q and Galileo E1-B modulations. Sampling from both GPS and Galileo would provide an enhancement to the number of observable reflections; and a secondary point of GNSS-R measurements.

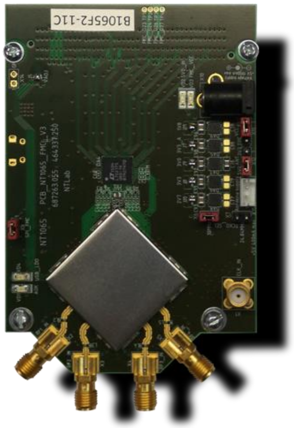

Figure 16. NT-1065 front end board. (NTLab 2017).

Finally, a digital signal processing stage is necessary to process the data from the NT1065 FE. The GNSS-R receiver implementation necessitates the processing of four independent receiving channels from the NT1065 front-end at sample rates of 53 Mhz. To ensure lightweight portability for airborne applications, the most logical choice for the digital processing platform is an integrated circuit board. This approach allows for efficient processing and integration of the multiple channels within a compact design. By utilizing an integrated circuit board, the receiver can effectively handle the processing requirements while maintaining the desired lightweight characteristics. Therefore, an integrated circuit board emerges as the ideal digital processing platform for the GNSS-R receiver implementation, considering the need for channel processing and lightweight operation.

The UltraScale ZCU104 FPGA Multi-processing system on a chip was selected as the integrated circuit for the overall GNSS-R receiver design and is shown in Figure 17. The ZCU104 chip combines a processor and a reconfigurable FPGA fabric, enabling software control over the hardware components of the chip (UltraScale 2017). This hardware allows for the efficient implementation of the concept of Software-Defined Radio (SDR) on a single chip. The FPGA performs basic arithmetic processing in parallel, such as accumulate and sum operations for correlation calculations, providing a higher throughput compared to a typical processor. The FPGA fabric was selected for performing DDM calculations and storing the results in memory for this receiver design. Two main reasons justify this choice. Firstly, the NT1065 front-end generates a minimum data size of 53,000 bytes per 1ms sample, and the ZCU104 FPGA offers fast memory with a throughput of up to 10 Gigabits/s on the fabric. This high-speed capability ensures efficient processing and storage of data from the front-end. Secondly, the compact form factor of the ZCU104 FPGA board makes it easily mountable onto aerial vehicles, facilitating its integration into airborne applications. The supplementary processors of the ZCU104 are used for peripheral management of other hardware components such as memory storage and FE configuration control.

Figure 17. Xilinx ZCU104 FPGA board (Xilinx 2021).

The key requirement of the payload is to generate DDMs in real-time, the operational process of generating DDM is described in Equation 15.

$$DDM(f_d, \tau) = \int_0^{T_s} S_r(t) C_r(t + \tau) e^{-j2\pi(f_d + f_c)t}\, dt \qquad \text{Equation 15.}$$

Here f_d is the Doppler frequency offset, τ is the delay, f_c is the centre carrier frequency and t is the coherent integration time in samples. A DDM is created by correlating the received signal S_r with a replica of the code C_r with combination of different Doppler frequency offsets and code delays. This process is repeated for the duration of the code period $T_s = \frac{1}{F_s}$ and for all possible delays. The received reflected signal is assumed to be weak and therefore the DDM is commonly averaged in-coherently to increase the signal power. This operation is shown in Equation 16.

$$DDM_{avg} = \frac{1}{N}\sum_{n=1}^{N} DDM\,(f_d, t, n) \qquad \text{Equation 16.}$$

Where N is the total number of DDMs averaged. The common value used for N is derived from the total number of code period samples that are contained in a duration of 1 second. The DDM can be calculated utilizing the previously described serial search method, where a replica for each possible combination of code delay and each possible Doppler frequency shift is generated and correlated with the received signal. Table 1 shows the parameters of each modulation and additionally the total sample size of each code period after the FE performs the digitization. From this table, it is concluded that applying the serial search technique would require an incredible number of repetitions to be performed, considering GPS L2C alone would require up to one billion repetitions to generate a full DDM due to the longer code period duration. Fortunately, the PCPS method that utilizes FFT to perform circular correlation reduces the repetitive calculations significantly. For more information regarding PCPS refer to Section 2.3.3.

Table 1. FFT Requirements for the conventional PCPS method.

Constellation	**GPS**	**GPS**	**GPS**	**Galileo**
Modulation	C/A	L2CA	L5I/Q	E1 OS
Frequency band	L1	L2	L5	L1
Code frequency (MHz)	1.023	1.023	10.23	1.023
Code Length	1023	10230	10230	4092
Minimum integration time (ms)	1	20	1	4
Minimum bandwidth (MHz)	2.046	2.046	20.46	8
Sample size per code	53,000	1,060,000	53,000	212,000
FFT minimum length required for PCPS @ Fs = 53 MHz	53,000	1,060,000	53,000	212,000

When planning to implement PCPS on the UltraScale ZCU104 FPGA device, it is essential to consider the required FFT size. Table 1 presents the minimum length for each FFT transform size, which is determined by multiplying a single 1 millisecond sample size by the minimum integration time of a modulation. Among the modulations, GPS L2C demands the largest FFT size of 1 million points. However, the ZCU104 platform's FFT functionality can only support a maximum FFT size of 65,536 points (UltraScale 2017). Thus, executing such a large FFT calculation on the target FPGA poses a significant technical challenge. Furthermore, the memory and storage requirements for storing FFT results between stages must be considered. Directly implementing such a substantial data processing size on the hardware would prove exceedingly difficult. Consequently, this work focuses solely on reducing the FFT and data processing size of the underlying acquisition algorithm.

Typically, researchers utilize the Cooley Turkey method to calculate large transformations using a subset of smaller FFTs (Oppenheim, 1999). However, the main drawback of such a configuration is that additional memory buffers are then required to handle data transfer between each stage. To overcome this issue, prior receiver designs utilized standalone dedicated FPGAs to perform these calculations and utilized a secondary FPGA for data handling and storage. An example of 1M FFT point implementation for GNSS-R is shown in Buist et al (2013). The drawback of this design is that adding a secondary FPGA board to the receiver would increase weight and consequently the size of the payload and introduce greater design complexity. Given the payload’s strict mass and volume budgets a single board solution is preferred instead.

Given the outlined considerations, a more efficient DDM processing methodology is required to meet the design objectives of the GNSS-R receiver payload. The complete and built miniaturized GNSS-R receiver would provide several key enhancements over existing designs. These enhancements are: 1) synchronous sampling of all 3 antenna channels through a singular FE, and 2) the subsequent real-time multi-constellation and multi-frequency DDM generation from the samples. The second enhancement therefore is the main motivation behind this work, and in the subsequent chapter, a novel DDM generation method is proposed which builds from prior GNSS signal acquisition research.

Chapter 3: FFT Optimized Software-based DDM Generation Methodology

In this chapter, an innovative signal processing method is presented for optimizing the implementation of software DDM generation. The inspiration for this method came from the need to have a real-time acquisition approach that is both computationally efficient and compatible with low-cost processing platforms. Previous research into computationally efficient acquisition methodologies has employed either reduced sample size techniques or piecewise FFTs to construct larger FFTs required for acquisition. This method aims to combine both techniques and is composed of three stages: resampling, partial correlation, and detection and decision. As a result, a multi-constellation and multi-frequency DDM generation processor is achieved. Additionally, the method utilizes a significantly shorter FFT transform size, reducing the system requirements for real-time implementation.

3.1 Signal Resampling

The last stage of the NT1065 FE digitally samples the four receiver chains with a sampling frequency of 53 MHz. This sampling frequency was chosen to ensure sampling and storing of the wideband L5 I/Q modulation with a bandwidth of 20.48 MHz. However, because the NT1065 FE outputs samples from a single ADC, GPS L1 C/A, GPS L2C, and Galileo E1-B modulations with smaller bandwidths are effectively oversampled. This results in more computation time for signal processing and leads to diminished returns. Additionally, more memory would be required for real-time implementation. Thus considering the limited memory of the FPGA, it would be beneficial to reduce the overall data size before DDM processing. As a solution to this problem, Zhang et al. (2018) proposed a methodology that utilizes the bandpass sampling theorem to down-sample the GPS L2C modulation. In this research, the bandpass sampling theorem was implemented to resample the GPS L1 C/A, GPS L2C, GPS L5 I/Q, and Galileo E1-B modulations to reduce the data size required for correlation. Although the technique has been implemented before, the novelty presented lies in the application of the technique to other modulations.

3.1.1 Band-pass Sampling Technique

For a single band signal, the range of sampling frequency is given by equation 17 (Vaughan et al 1991):

$$\frac{2F_U}{n} \leq F_s \leq \frac{2F_L}{n-1} \qquad \text{Equation 17.}$$

where F_U and F_L are the upper and lower cutoff frequencies, respectively, and n is a positive integer. The relationship between the sampling frequency F_s and the upper frequencies is such that, by sampling a time-continuous signal with frequency F_s, the frequency spectrum of the sampled sequence will not alias. Therefore, with the appropriate sampling frequency, the expanding components of the sampled sequence do not overlap with the frequency spectrum of the original signal within $[F_L, \ F_U]$. Using this principle, a resampling filter has been conceptualized in software and described next.

3.1.2 Sample Filter and Bandpass Filter Design

To effectively resample a modulation, a bandpass filter is designed to extract the signal around the useful bandwidth of the modulation, as described in section 2.2.1. The filter is designed with the following parameters as shown in Equation 18.

$$F_U = F_{IF} + \frac{B}{2}$$
$$F_L = F_{IF} - \frac{B}{2}$$
$$\omega_p = \left[\frac{2F_L}{F_s} - \Delta\omega_f\,, \frac{2F_U}{F_s} + \Delta\omega_f\right]$$

Equation 18.

where F_{IF} is the intermediate frequency, B is the bandwidth, F_L and F_U are the lower and upper cutoff frequencies of the main lobe, and F_s is the conventional sampling frequency from the front-end. ω_p is the vector of the normalized cutoff frequencies. $\Delta\omega_f$ is the margin parameter, which ensures the main lobe of the signal is sufficiently isolated. The bandpass filter is designed as an N-order Hamming-window, linear-phase, finite impulse response (FIR) filter (Oppenheim, 1999). By utilizing a bandpass filter on the broadband signal, only the main lobe located in the useful bandwidth of the modulation is preserved. This is an important step, as this foundational filter block prevents frequency aliasing.

After filtering with a band-pass filter, the main lobe should be sufficiently isolated and preserved. To reduce the sample size and effectively lower the sample frequency, a resampling filter was also designed. The resample filter design parameters are described in equation 19.

$$F_{du} = F_{IF} + \frac{B}{2}$$
$$F_{dl} = F_{IF} - \frac{B}{2}$$
$$n = floor(\frac{F_{du}}{B})$$

Equation 19.

where F_{du} and F_{dl} represent the upper and lower cutoff frequencies of the band-pass filtered signal. By utilizing Equation 17 and substituting the values of F_{du} and F_{dl} for F_U and F_L, respectively, the range of acceptable sampling frequencies can be found. The centre, or otherwise known as the resampling frequency, F_r, is given by equation 20.

$$F_r = \frac{F_{du} + F_{dl}}{2} \qquad \text{Equation 20.}$$

Because the new resampling frequency is reduced from the original sampling frequency F_s, the original intermediate frequency is also reduced due to the filter (Borre et al 2007). Equation 21 shows the calculation of the lowered intermediate frequency F_{dIF}.

$$F_{dIF} = Mod(F_{IF}, Fr) \qquad \text{Equation 21.}$$

To reduce the overall length of the digital sample, the band-pass filtered signal sequence is passed through the resample filter. The resample filter preservers every H-th index. Equation 22 shows the calculation for H, which is the ratio of the original sampling frequency Fs and the new resampling frequency Fr. This process creates a new, smaller digital sample with a new length L_r. The calculation for L_r is shown in equation 23, where L_r is the length of the resampled sequence, and L is the length of the original sequence. By applying the band-pass technique as presented, the new resampled sequence is reduced in length, yet still sufficient to reconstruct the signal.

$$H = ceil(\frac{Fs}{Fr})$$ Equation 22.

$$L_r = floor(\frac{L * Fr}{Fs})$$ Equation 23.

In the design of this payload, the front-end supplies up to 4 antenna channels and can capture the entirety of the GNSS spectrum. Therefore, only 4 modulations are chosen to be acquired. Each modulation has its own unique band-pass filter, the parameterization of which is shown in Table 2. Initially, the incoming signal is filtered by a finite impulse response (FIR) pass-band filter and then resampled. By resampling the original incoming signal and isolating each individual main lobe of a specific modulation, the total sample size is reduced. However, because only the main lobe of the signal is kept, and the sidebands are removed, a loss of 1 dB is experienced in real scenarios (Zhang et al., 2018). Additionally, although the total sample size is reduced, this reduction is only for a single sample of 1 millisecond. This reduction is an issue for the conventional method, as its computational complexity of FFT calculations is dependent on code period duration. This situation is undesirable when considering modulations that contain longer code durations, for example, GPS L2C that has a 20-millisecond code period. Therefore, the dependence of the FFT size on the code period must be considered such that the implementation can be feasibly realized on the target hardware platform.

3.2 Partial Correlation

Lin et al. (1999) developed an application of partial circular correlation for GNSS acquisition, specifically targeting the efficient acquisition of the exceptionally long GPS L1 P(Y)-code. This method, known as Double Block Zero Padding (DBZP), relies on the use of partial correlators with durations equivalent to tenths of a code period, referred to as "blocks." Foucras et al. (2012) conducted an analysis of DBZP and concluded that it introduces several key enhancements, addressing issues such as DBZP bit transition sensitivity and Doppler frequency degradation, which affect acquisition performance. They named this improved version Double-Block Zero Padded Transition Insensitive (DBZPTI). However, the evaluation of DBZPTI was limited to simulated Galileo E1-B data and has not been applied to other modulations.

In this thesis, DBZPTI method is adopted and implemented for two reasons. 1) Bit transitions occur when there is a change in navigation data bits, resulting in destructive summations during correlation that serve no useful purpose in processing. Considering that GPS L2 CM, L5 I/Q, and Galileo E1-B have a data bit duration equal to the code period, there is a 50% chance of a bit transition occurring during the correlation period. And 2) the DBZPTI method offers efficient processing of longer codes, making it suitable for the more efficient processing of the 20-millisecond-long GPS L2C code compared to the PCPS method. The DBZPTI method alleviates the requirement of processing the whole code period at once by splitting it into smaller subsequent sections, effectively deconstructing the large code period samples into smaller blocks of code. This feature, along with its benefits in handling bit transitions, makes DBZPTI the preferred method of correlation due to its reduced data processing requirements. While the DBZPTI method has been implemented in prior literature, the novelty of this research lies in its application and analysis of this method to GPS L2 CM and L5 I/Q modulations as well as the GPS L1 C/A-code, which set it apart from prior literature. The next subsection details the DBZPTI methodology.

3.2.1 Double-Block Zero Padded Transition insensitive method

The first step is to create a vector with two complete code period samples (t_{coh}) of the incoming signal. The vector sample is multiplied by a local carrier wave replica to create the baseband in-phase (I) and quadrature phase (Q) components. The replica carrier wave is generated without any Doppler frequency compensation, so only two replicas are required. The baseband components I and Q are split into 2M blocks of N samples and are concatenated together to form two adjacent blocks. Equation 24 describes the formulated digital baseband I and Q vectors of the sampled signal $\mathrm{s}(t)$, F_{If} is the intermediate frequency of the sampled signal, and k is the sample index.

$$I(k) = s(t) * sin\left(2\pi F_{If} t\right) \qquad \text{Equation 24.}$$
$$Q(k) = s(t) * cos(2\pi F_{If} t)$$

The second step is to generate a local replica with the duration of a complete code period, t_{coh}. The code replica is split into 2M blocks of N samples, and each of the 2M code replica blocks is then concatenated with a zero-padded block of equivalent size N. In total, the equivalent code replica matrix will have a total length of two complete code period samples. The complex vector is shown in Equation 25 where $x(k)$ becomes the input to the following FFT function.

$$x(k) = e^{(I(k)+jQ(k)} \qquad \text{Equation 25.}$$

The third step performs correlation on each 2M block of the $I(k)$ and $Q(k)$ components with a 2M zero-padded code block of the local replica. Figure 18 illustrates the correlation procedure, where 2M blocks of both I and Q are combined to form a complex vector. The complex vector $x(k)$ is the input to the following FFT function.

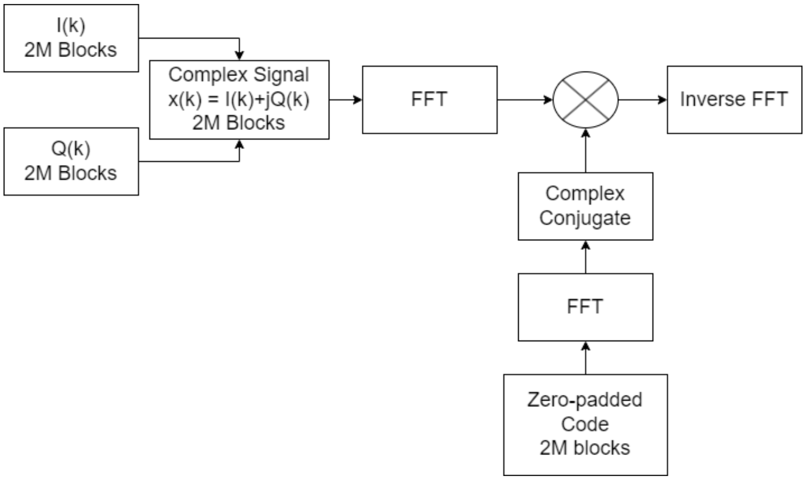

Figure 18. Proposed method correlation of signal samples utilizing FFT.

The local zero-padded code block is transformed into the frequency domain via FFT, and its complex conjugate is calculated. The complex vector $x(k)$ and the local complex code replica blocks are then multiplied and an inverse FFT of the result is performed. The resulting correlation represents a partial correlation of the total sample for a delay range corresponding to $[(m-1) \times t_{block}, m \times t_{block}]$, where m represents the block number.

Because of the zero-padding on the code block, the second portion of the inverse FFT results do not provide any useful information, so only the first portion of the total 2N correlation result is retained. This process is repeated M times to create an N by M matrix, where each column contains the M partial correlation for the same code delay step Δt.

In the last step, the Doppler frequency shifts are estimated by performing an FFT on each column of the partial correlation matrix. The FFT is zero-padded to the next power of 2 to increase the sampling resolution and improve the accuracy of the Doppler frequency shift estimate. This step is done to counteract the degradation of the correlation caused by initial low sampling resolution without padding (Foucras et al. 2013). By using Radix-2 FFT algorithms, the calculation time complexity is reduced (Pell et al. 2006). Only M blocks of the FFT result are kept maintaining the same number of rows.

The entire process is repeated until all 2M signal blocks of $\mathrm{I(k)}$ and $\mathrm{Q(k)}$ have shifted by one block and all blocks have been shifted through. The code block replicas remain unchanged. Once all the blocks have been shifted, the resulting matrix will contain a total of N columns, equivalent in length to $t_{coh} \times F_s$, and a total of M rows. The resulting matrix represents a 2-dimensional search space, where the rows represent the frequency bin, and the columns represent the code delay. The frequency resolution of the bin is dependent on the integration time, t_{coh} , and is given as $\Delta f = \frac{1}{t_{coh}}$. The code resolution, on the other hand, is dependent on the sample frequency F_s and is given by Δt. The final Doppler frequency estimation F_d is given by $F_d = k \times \Delta f, k \in [1..M]$. A summary of the parameters used in this method can be found in Table 2.

Table 2. List of parameters for proposed methodology.

Doppler frequency interval (Hz): $[-F_{max}, F_{max}]$
Coherent integration time (ms): t_{coh}
Number of blocks: M = $(2F_{max} * t_{coh})$
Size of block: N = $\frac{F_s * t_{coh}}{M}$
Duration of block (ms): $t_{block} = \frac{1}{t_{coh}}$
Code delay step (ms): $\Delta t = \frac{1}{F_s}$

3.3 Signal Detection and Decision

A general detection process involves identifying a desired signal within a set of noisy data. The received signal from a GNSS satellite is often obscured by noise. By post-processing the noisy signal and comparing it to a threshold, a test can be performed to establish the presence of a signal, also known as the test statistic. Before detection, the DDM from the correlation results is extracted. The correlation magnitude reflects the relationships between each individual code delay and Doppler frequency shift. To determine the presence of a useful signal, a detection threshold is set, and a comparison is made with the highest correlation peak. If the threshold is exceeded, the signal is deemed present. Referring to Equation 15, the resulting row and column indices of the peak represent the code delay and coarse Doppler frequency estimates.

The Neiman-Pearson hypothesis test is used to determine the presence of a useful signal by comparing the correlation magnitude to a detection threshold (Schonhoff et al 2006). The threshold is set based on the desired probability of false alarm and probability of detection. The test statistic is the maximum correlation peak and if it exceeds the threshold, the signal is declared present. The resulting row and column indices of the peak represent the code delay and coarse Doppler frequency estimates. This approach is particularly useful in GNSS signal detection as the noise is assumed to be Gaussian, and the received signal is considered under two hypotheses: H_0 the null hypothesis (no useful signal is present, only noise is present) and H_1 the alternative hypothesis (useful signal is present). This method allows for a precise characterization of the signal detection problem and can be used to optimize the detection performance.

The detection of reflected signals can be a challenging task, as the signal strength is significantly attenuated during the reflection process. To overcome this issue, researchers have employed in-coherent integration, a technique that boosts the signal strength in post-processing before detection (Park, et al 2014). This process is especially important for the payload as its primary objective is to acquire reflected signals. To ensure that the correct PRN is detected in the reflected signal, it is crucial to determine the correct threshold for positive detections. This work assumes that the reflected signals are maximally attenuated by -10 dB from the nominal transmit power and aims to detect them with a probability of 90%. Once a reflected signal is successfully detected, a longer 1-second in-coherent integration can be performed to generate the DDM observations. The threshold for positive detections is derived based on the Neiman-Pearson hypothesis test, and the number of in-coherent steps is determined to reduce the chances of false detections and increase the chances of successful detections, resulting in a more efficient receiver. In the following section, the method for generating the test statistic and determining the threshold will be discussed in more detail.

3.3.1 Reflected Signal Detection

Post-acquisition, the generalized output from DBZP is given by (Lin et al 1999).

$$I_x^2(k) + Q_x^2(k) = \frac{A^2}{4} M^2 R^2\big(e_t(i)\big) sinc^2\left(\frac{\pi t_{coh}}{M} f_d\right) \frac{sinc^2(\pi(m - f_d t_{coh}))}{sinc^2(\frac{\pi(m - f_d t_{coh})}{M})} \qquad \text{Equation 26.}$$

where A is the amplitude of the signal, M is the number of blocks, R is the code autocorrelation function, $e_t(i)$ is code delay error, for ith delay, m is the point at which the FFT is taken, f_d represents the Doppler frequency and t_{coh} is the coherent integration time.

3.3.1.1 Detection Threshold Derivation

The H_0 Null Hypothesis assumes the noise is Gaussian and additionally the correlator outputs $I_x^2(k),\ Q_x^2(k)$ are independent standard normal random variables. Equation 27 represents the null hypothesis detector.

$$H_0 = \sum_{k=1}^{K} N_I^2(k) + N_Q^2(k) \qquad \text{Equation 27.}$$

where $\sigma_{N_{I,Q}}^2$ is the variance of the noise, *K* is the in-coherent integration factor and N_x^2 is the noise from the in phase and quadrature components of the signal. By integrating multiple outputs of the detector over multiple code periods, the detector's sensitivity increases. The noise is assumed to be white and Gaussian, therefore its variance can be determined from the final output of equation 26 when only noise is present, as given by equation 28.

$$\sigma_{N_{I,Q}}^2 = \frac{M^2 N_0}{2t_i} \qquad \text{Equation 28.}$$

Therefore, the probability density function of the noise is equivalent to a Gaussian Normal distribution with a zero-mean given by equation 29.

$$N_I^2(k),\ N_Q^2(k) = N(0,2\sigma_{N_{I,Q}}^2) \qquad \text{Equation 29.}$$

Then the normalized detector is therefore can be derived as shown in equation 30, where D_0 represents the correlation magnitude.

$$\frac{H_0}{2\sigma_{N_{I,Q}}^2} = \sum_{k=1}^{K} \frac{1}{2\sigma_{N_{I,Q}}^2} \left(N_I^2(k) + N_Q^2(k)\right)$$

Equation 30.

This detector becomes an equivalent to a chi-squared distribution with $2K$ degrees of freedom, where K is the in-coherent integration factor shown in Equation 31.

$$\frac{\mathrm{D}_0}{2\sigma_{N_{I,Q}}^2} \sim \chi^2(2K)$$

Equation 31.

The threshold value T_H can be used as a decision boundary for detection, where if the magnitude of the peak exceeds the threshold, the signal is declared present. The probability of a false alarm is the probability that a detection is made, but only noise is present. By determining the threshold value T_H for a pre-defined probability of false alarm, the receiver can be made more efficient by reducing the chances of false detections and increasing the chances of successful detections. By inverting the distribution for a pre-defined value of false alarm probability, the relevant threshold value T_H can be determined as represented in equation 32. $\chi^2(2K)$ is a centralized chi-squared distribution with $2K$ degrees of freedom in-coherent integrations and Z is the magnitude under test.

$$P_{fa} = P_{H_0}(H_1) = P_{H_0}(H_0 > T_H)$$

$$= P_{H_0}\left(Z > \frac{T_H}{2\sigma^2_{N_{I,Q}}}\right), Z \sim \chi^2(2K)$$

Equation 32.

3.3.1.2 Probability of Detection

The alternative hypothesis, H_1, posits that a useful signal exists within the sample and the magnitude of the peak of the correlation can be expressed when this is the case using Equation 33.

$$H_1 = \sum_{k=1}^{K} I^2(k) + Q^2(k)$$

Equation 33.

The correlator outputs $I(k)$ and $Q(k)$ are assumed to be independent, standard normally distributed with a non-zero mean of λ and a variance of $2\sigma^2_{N_{I,Q}}$, shown in Equation 34.

$$I(k), Q(k) = N(\lambda, 2\sigma^2_{N_{I,Q}})$$

Equation 34.

The normalized test statistic therefore is shown in equation 35, the correlator outputs are normalized by the $\sigma^2_{N_{I,Q}}$ noise variance from equation 26.

$$\frac{H_1}{2\sigma^2_{N_{I,Q}}} = \sum_{k=1}^{K} (\frac{I(k)}{\sqrt{2\sigma^2_{N_{I,Q}}}})^2 + (\frac{Q(k)}{\sqrt{2\sigma^2_{N_{I,Q}}}})^2 \qquad \text{Equation 35.}$$

It is assumed that the outputs of the correlator, I(k) and Q(k), are independent. Therefore, the sum of their squares, as shown in Equation 36, can be modeled by a chi-squared distribution with $2K$ degrees of freedom and a non-centrality parameter λ, where K represents the number of in-coherent integration steps.

$$\frac{H_1}{2\sigma^2_{N_{I,Q}}} = \chi^2(2K, \lambda) \qquad \text{Equation 36.}$$

Where λ, the non-centrality parameter of the chi-squared distribution is described by equation 37. The non-centrality parameter is the sum of the squares of mean of each the correlator output.

$$\lambda = \sum_{k=1}^{K} \lambda^2_{k,I}(k) + \lambda^2_{k,Q}(k) \qquad \text{Equation 37.}$$

Therefore, mean of the summation can be derived from the expected values of the normalized correlator outputs $I(k)$ and $Q(k)$ as shown in equation 38. Therefore, λ can be rewritten as the output of the correlator from equation 24 $I(k)$ or $Q(k)$ as show in equation 39.

$$\lambda_{k,I} = E\left[\frac{I(k)}{\sqrt{2\sigma_{N_I}^2}}\right] \lambda_{k,Q} = E\left[\frac{Q(k)}{\sqrt{2\sigma_{N_Q}^2}}\right]$$ Equation 38.

The non-centrality parameter, λ, of the chi-squared distribution is described by equation 37. It is the sum of the squares of the means of each of the correlator outputs. The mean of the summation can be derived from the expected values of the normalized correlator outputs $I(k)$ and $Q(k)$ as shown in equation 38. Therefore, λ can be rewritten in terms of the output of the correlator, $I(k)$ or $Q(k)$, as shown in equation 39.

$$\lambda = \frac{KA^2}{2\sigma_{N_{I,Q}}^2} M^2 R^2\big(e_t(i)\big) sinc^2\left(\frac{\pi t_i}{M} f_d\right) \frac{sinc^2(\pi(m - f_d t_i))}{sinc^2(\frac{\pi(m - f_d t_i)}{M})}$$ Equation 39.

Thus, a threshold is derived by applying the test statistic $\frac{H_1}{2\sigma_{N_{I,Q}}^2}$, therefore the detector can be modeled by a chi-squared distribution with $2K$ degrees of freedom and a non-centrality parameter λ. This allows for the derivation of the probability of detection, which is the probability that a signal is detected. The probability of detection for the detector is shown in equation 40.

$$P_d = P_{H_1}(H_0) = P_{H_1}(H_1 > T_H)$$
$$= P_{H_1}\left(Z > \frac{T_H}{2\sigma_{N_{I,Q}}^2}\right), Z \sim \chi^2(2K, \lambda)$$ Equation 40.

Therefore, the probability of detection depends on the received signal strength. Additionally, the non-centrality parameter λ is dependent on the Doppler frequency shift f_d. Therefore, careful consideration must be taken when deriving a global average probability of detection. By constraining the probability distribution function, the performance of acquisition can be modelled by varying the received power and setting the probability of detection to a constant value to find K, the number of non-coherent integrations required to achieve the desired probability of detection for the given received power.

3.4 Software Implementation

The proposed methodology evaluation was implemented using software developed in MATLAB. This choice was made due to the integrated workflow environment that MATLAB provides, allowing for verification of the strategy before it was ported to a standalone C executable using the MATLAB “Coder” toolbox. The C programming language was chosen for its portability across various processing platforms and development environments. The software was specifically designed to process raw data acquired from the NT1065 front-end, with a fixed sampling frequency of 53 MHz and IF carrier frequency derived from the NT1065 front-end configuration. The raw data samples were provided with a 2-bit resolution and were converted to a signed integer notation for processing. Figure 19 shows the block diagram of the software processing.

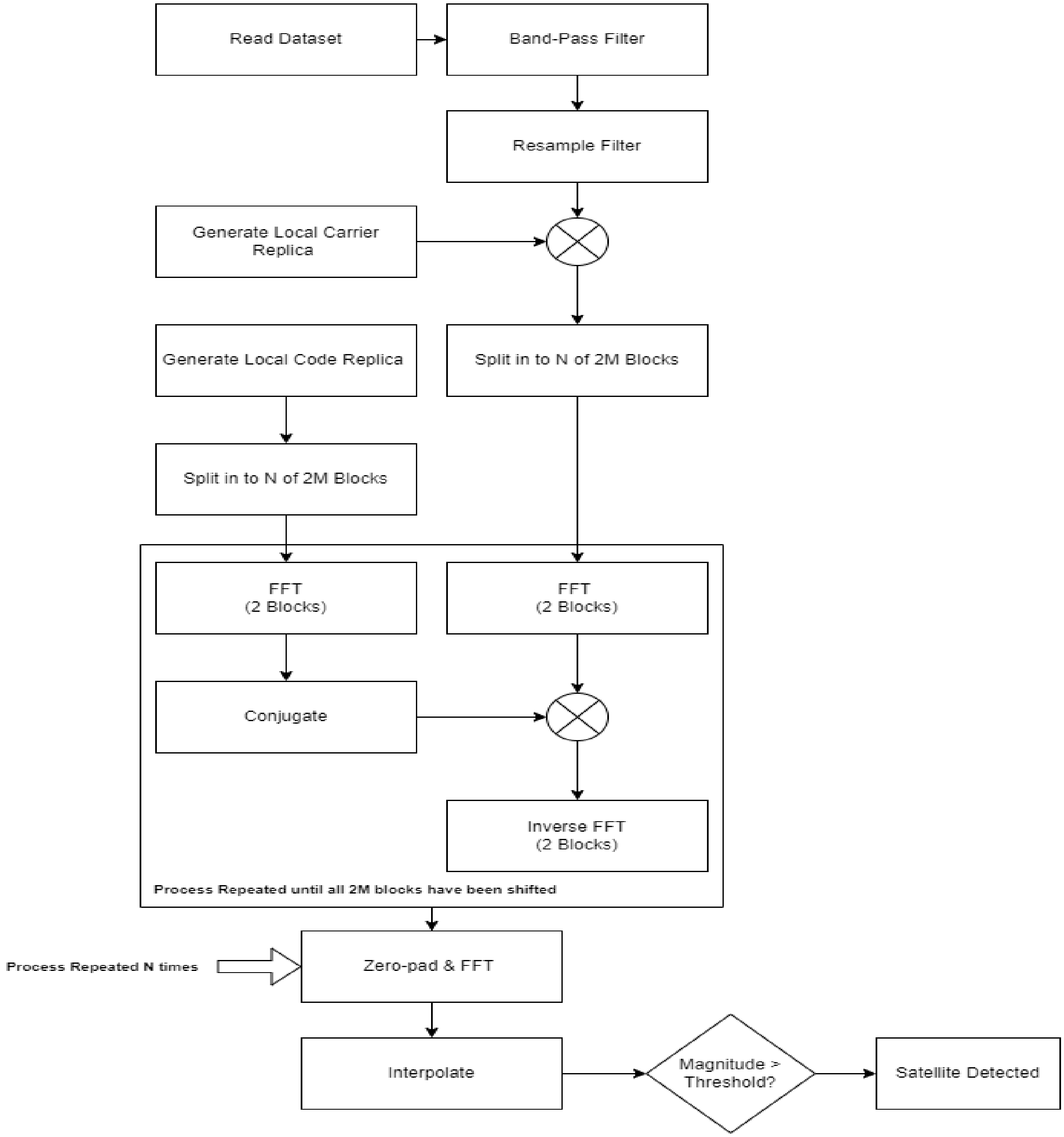

Figure 19. Software implementation pseudocode diagram.

The software process begins by reading in a dataset of digital RF data, as shown in Figure 19. The size of the data is dependent on the chosen modulation, and the software configuration parameters for each modulation are outlined in Table 3. It is important to note that the initial data size from the front-end remains the same for both the PCPS and the proposed method. However, unlike in PCPS, the data is filtered and reduced in the proposed method. The initial size of the data sample is derived from the NT1065 front-end configurations "ConfigSet1.hex" and "ConfigSet2.hex" (Tcherniakovski et al., 2016; NTLAB, 2016). These configurations are determined based on factors such as the sample frequency, intermediate The minimum required data are equivalent to two fully sampled code periods, as shown in Table 3, where the second column represents the duration in milliseconds and the third column represents the total data size.

Table 3. Proposed acquisition strategy parameterization.

Modulation	t_{coh} **(ms)** F_{IF} **(MHz)**	**Total Size:** $t_{coh} * 2 * F_s$	**Resample Filter Parameters (MHz)**	**Total Down Sampled Size** F_{max}**= 20 KHz**	**Final FFT with zero-padding**
GPS L1 C/A-code	1 14.58	106,000	F_u= 15.603 F_L= 13.556 ω_p= [0.4871,0.6133] F_r= 3.8871	7840 $2N = 196$ $M = 40$	64
GPS L2 CM	20 7.40	2,120,000	F_u= 8.432 F_L= 6.377 ω_p= [0.2161,0.3423] F_r= 4.2314	169,600 $2N = 212$ $M = 800$	1024
GPS L5 I/Q	1 13.55	106,000	F_u= 23.78 F_L= 3.32 ω_p= [0.1008,0.9219] F_r= 47.56	95,120 $2N = 2378$ $M = 40$	64
Galileo E1-B	4 14.58	424,000	F_u= 16.603 F_L= 12.557 ω_p= [0.4493,0.6511] F_r= 8.3364	66880 $2N = 418$ $M = 160$	256

The dataset is initially filtered by a band-pass filter to isolate the useful bandwidth component. The filter was designed using a Hamming window, based on the materials from Tan et al

(2019), and is a 48th-order finite impulse response bandpass filter with linear phase and zero initial condition. After band-pass filtering, the signal is down sampled by the resample filter to reduce the initial sampling frequency of 53MHz to F_r, the new lowered sampling frequency. The third column of Table 3 describes the band-pass filter parameters for each of the modulations, while the fourth column describes the down-sampled data size. The implementation of these steps ensures that only relevant data is processed, resulting in a more efficient and accurate acquisition process.

Next, a carrier replica is generated at the intermediate frequency. Unlike in PCPS acquisition, this process is only done once, as the replica does not need to be compensated for the Doppler frequency. Additionally, a full code period of the code replica is generated. For GPS L1 C/A-code, L2C and L5 I/Q, linear feedback shift registers are used to generate the code, as described in Chapter 2. For Galileo E1-B, the memory codes have been retrieved from (ESA 2022) and stored in memory as a header filter.

After generating the carrier and code replicas, the resampled data are mixed with the carrier replica to produce the in-phase and quadrature baseband components. These baseband components are then segmented into two M blocks, and the code replica is zero-padded to create equivalent 2M code replica blocks. Subsequently, partial correlation is performed on each M block using FFT, and this process is repeated $2M$ times. Conveniently, these FFT calculations can be performed in parallel as well as each partial correlation is independent of one another.

This results in a N by M matrix, from which a zero-padded FFT is taken of each Nth column. The zero-padding is performed to ensure that the size of the FFT vector $2M$ is the next power of 2. The fifth column of Table 3 shows the amount of zero-padding performed for each modulation. Since the last FFT zero-padding effectively produces a larger oversampled vector, an interpolation is performed to reduce the result to the original size of M. The interpolation method used is the Dirichlet Kernel, which can be found in Ouimet (2022). After the interpolation, the result is a matrix of size N by M, where the rows represent the Doppler frequency, and the columns represent the code delay. By analyzing this matrix, the largest peak is then extracted. If the magnitude of the peak is greater than the set threshold, a satellite detection is confirmed, and the resulting row and column represent the frequency and code delay of the detected satellite. This approach ensures that the correlation process is accurate and efficient, leading to improved satellite detection performance.

To verify the proposed acquisition strategy for comparison, the conventional PCPS method was also implemented as described in Figure 15 from Section 2.2 using MATLAB. Equation 41 describes the total FFT calculations for each method, and Table 4 summarizes the parameters, the data size, as well as the maximal FFT transform sizes for each acquisition strategy and the total number of FFT repetitions necessary for processing a single satellite. Table 5 quantifies each FFT operation as additions and multiplications. This structure allows for a direct comparison of the performance and computational requirements of the two methods.

$$\begin{cases} Repetitions\ FFT\ Proposed\ Acquisition\ Strategy = 6M + \frac{2N}{2} \\ Repetitions\ FFT\ PCPS = 3 * \frac{F_{max}}{250} \end{cases} \qquad \text{Equation 41.}$$

Table 4. Conventional method and proposed acquisition strategy FFT transform size comparisons.

Modulation	Date size for PCPS	Data size for proposed method	Maximal FFT transform for PCPS	Maximal FFT transform for proposed method	Total FFT operations for PCPS	Total FFT operations for proposed method
GPS L1 C/A-code	53,000	7,774	53,000	196	243	4040
GPS L2C	1,060,000	84,628	1,060,000	1024	243	84,920
GPS L5 I/Q	53,000	47,560	53,000	2378	243	47,680
Galileo E1-B	212,000	33,346	212,000	418	243	33,920

Table 5. Conventional method and proposed acquisition strategy number of additions and multiplications per FFT comparisons.

Modulation	Number of multiplications per FFT for proposed method $O(\frac{N}{2}\sqrt{\log_2 N})$	Number of Additions per FFT for proposed Method $O(N\sqrt{\log_2 N})$	Number of multiplications per FFT for PCPS $O(\frac{N}{2}\sqrt{\log_2 N})$	Number of Additions per FFT for PCPS $O(N\sqrt{\log_2 N})$
GPS L1 C/A-code	104,980	209,960	270	540
GPS L2C	2,371,158	4,742,316	1619	3,238
GPS L5 I/Q	104,980	209,960	3,981	7,963
Galileo E1-B	445,880	891,754	616	1,233

The proposed methodology for the acquisition strategy involves measuring the total number of FFT calls, which is the sum of N repetitions of the final FFT and 2M repetitions during each partial correlation. Specifically, a total of 3 FFT transforms are performed per M block, resulting in a total of 6M FFT transforms. In comparison to the PCPS method, the proposed strategy requires more repetitions but offers a significantly smaller size for each FFT transform. Furthermore, as shown in Table 5, the proposed strategy effectively reduces the number of additions and multiplications due to the reduced FFT length. Consequently, the FFT transforms in the proposed strategy are computed faster than those in the PCPS method. In the following chapter, a comprehensive comparison of the performance of each acquisition strategy is presented, considering factors such as direct signal reception and their respective execution time.

Chapter 4: Acquisition Strategy Tests and Analysis

This chapter presents the hardware simulator used to test the proposed acquisition method and compares its results to those of the conventional method. The sensitivity and accuracy of the proposed method are analyzed and the results of a Monte Carlo simulation for weak-signal analysis are also presented. The simulation results demonstrate the effectiveness and efficiency of the proposed method in acquiring weak signals.

4.1 Test Hardware Setup

To verify the functionality of the proposed processing methodology, a simulation was conducted using the Spirent GSS9000 GNSS simulator. The NT1065 front-end was used to capture raw data from the simulator's coaxial cable and digitize it. The digitized data were then supplied as signed 2-bit samples to a computer running MATLAB, which was configured with an Intel Hexa-Core Core i9-9900K CPU and 16 gigabytes of RAM. The NT1065 lab front-end was configured according to the manufacturer's provided configuration files (NTLab 2016). To capture GPS L1 C/A-code, GPS L2C, and Galileo E1-B signals, the configuration file "ConfigSet01.hex" was used, and "ConfigSet02.hex" was used to capture GPS L5I/Q signals, although the sampling frequency was modified to be the same 53 MHz for both configurations. Figure 20 describes the configuration file parameters.

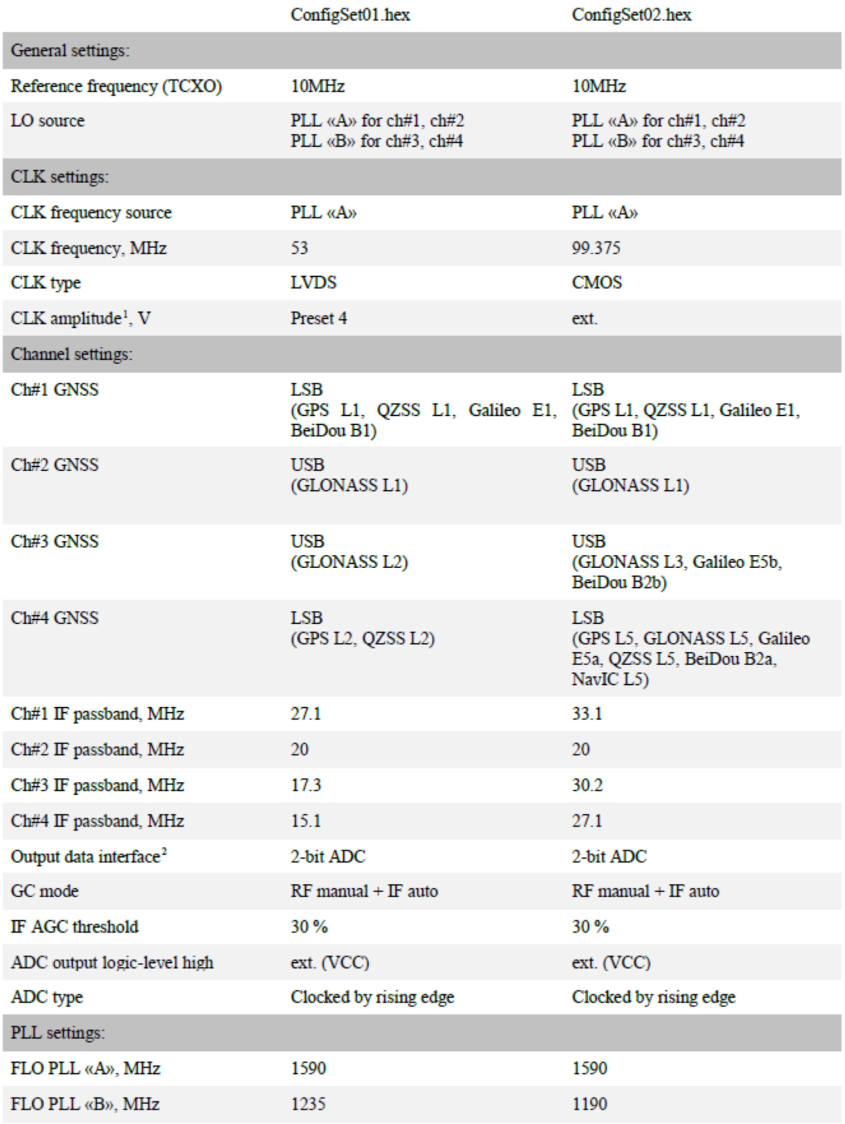

	ConfigSet01.hex	ConfigSet02.hex
General settings:		
Reference frequency (TCXO)	10MHz	10MHz
LO source	PLL «A» for ch#1, ch#2 PLL «B» for ch#3, ch#4	PLL «A» for ch#1, ch#2 PLL «B» for ch#3, ch#4
CLK settings:		
CLK frequency source	PLL «A»	PLL «A»
CLK frequency, MHz	53	99.375
CLK type	LVDS	CMOS
CLK amplitude[1], V	Preset 4	ext.
Channel settings:		
Ch#1 GNSS	LSB (GPS L1, QZSS L1, Galileo E1, BeiDou B1)	LSB (GPS L1, QZSS L1, Galileo E1, BeiDou B1)
Ch#2 GNSS	USB (GLONASS L1)	USB (GLONASS L1)
Ch#3 GNSS	USB (GLONASS L2)	USB (GLONASS L3, Galileo E5b, BeiDou B2b)
Ch#4 GNSS	LSB (GPS L2, QZSS L2)	LSB (GPS L5, GLONASS L5, Galileo E5a, QZSS L5, BeiDou B2a, NavIC L5)
Ch#1 IF passband, MHz	27.1	33.1
Ch#2 IF passband, MHz	20	20
Ch#3 IF passband, MHz	17.3	30.2
Ch#4 IF passband, MHz	15.1	27.1
Output data interface[2]	2-bit ADC	2-bit ADC
GC mode	RF manual + IF auto	RF manual + IF auto
IF AGC threshold	30 %	30 %
ADC output logic-level high	ext. (VCC)	ext. (VCC)
ADC type	Clocked by rising edge	Clocked by rising edge
PLL settings:		
FLO PLL «A», MHz	1590	1590
FLO PLL «B», MHz	1235	1190

Figure 20. Configuration sets "ConfigSet01.hex" and "ConfigSet02.hex" parameters (NTLab 2016).

Table 6 shows the frequency resolutions and code delay resolutions for both methodologies for each of the given modulations. The PCPS method serves as a basis for comparison with the proposed methodology's acquisition detection performance. For PCPS, the Doppler frequency step was fixed at 250 Hz for all modulations, while for the proposed methodology, the Doppler frequency step varies with the coherent integration time. And the code delay resolution is the same for both methods. The next section describes the GSS9000 simulation description.

Table 6. Doppler frequency resolutions and code delay resolutions for PCPS and proposed method.

Modulation	**Doppler frequency resolution (Hz)**		**Code delay resolution**		**Resampling factor** $\boldsymbol{H = F_s/F_r}$
	PCPS	**Proposed Method**	**PCPS**	**Proposed Method**	**Proposed Method**
GPS L1 C/A-code	250	$t_{coh} = 1\,ms$ $\triangle F_{doppler} = \frac{1}{tcoh} = 1000$	$\triangle t = \frac{1}{Fs}$		13.64
GPS L2C		$t_{coh} = 20\,ms$ $\triangle F_{doppler} = \frac{1}{tcoh} = 50$			12.5
GPS L5I/Q		$t_{coh} = 1\,ms$ $\triangle F_{doppler} = \frac{1}{tcoh} = 1000$			1.11
Galileo E1-B		$t_{coh} = 4\,ms$ $\triangle F_{doppler} = \frac{1}{tcoh} = 250$			6.36

4.1.2 GSS9000 Simulator Scenario Description

The Spirent GSS9000 in the GNSS Laboratory is an advanced and highly accurate GNSS signal simulator that can simulate GPS L1, L2, and L5 modulations, as well as Galileo E1. The simulator provides raw analog signals as if captured by a GNSS antenna, effectively simulating a GNSS antenna and supplying the raw data through a coaxial cable (Spirent, 2022). The GSS9000 simulator is configured using the provided SimGEN software, which allows for the creation of simulation scenarios with a wide range of modifications including both stationary receiver and a moving vehicle. For this simulation, a stationary receiver option was selected.

The default configurations for each GNSS modulation were chosen, the simulation defines the default configuration according to the original specifications outlined in the constellation's signal in space interface documentation (Spirent, 2022). Additionally, the default omnidirectional antenna with no additional in-line gain option was selected. No other configurations were made, and all other modulation transmit settings were kept at their default values. Table 7 shows the default nominal reference received power for each constellation, as configured in the simulator.

Table 7. Nominal received power for each modulation.

Modulation	**GPS L1 C/A-code**	**GPS L2 CM**	**GPS L5 I/Q**	**Galileo E1-B**
Received nominal power (dBm)	-128	-131	-127	-127

4.2 Direct Signal Acquisition

To verify the accuracy of the proposed method, a direct signal acquisition test was performed. A direct signal refers to a signal that is captured by the RHCP upward-facing antenna of the payload without experiencing multipath or attenuation. The GSS9000 simulator was configured to transmit each modulation at its defined nominal signal strength power, as shown in Table 7. Additionally, all 32 satellites of each constellation were turned on to transmit. To obtain a sufficient data set for analysis, the direct signal acquisition scenario was simulated for 30 seconds, and the total duration captured for each modulation was processed in MATLAB. Both the proposed acquisition strategy and PCPS were used for processing, while the GSS9000 simulator served as the truth data to verify acquisitions.

The software configurations for the proposed acquisition strategy for each modulation are described in Table 3. For both acquisition methods, it is assumed that the maximal Doppler frequency is between the ranges of -10 to 10 KHz. From Table 3, this resulted in 81 frequency bins for PCPS. From Table 3, the value of M is 40 for GPS L1 C/A-code and GPS L5 I/Q, corresponding to 40 frequency bins, respectively. To maintain consistency with PCPS, the theoretical maximal Doppler frequency uncertainty was increased such that 80 frequency bins could be formed.

Figure 21 describes the Doppler frequency bin spread on the Y-axis of the resulting DDM for the PCPS method, where F_{max} is 10 KHz, and the bins are spread decreasing from left to right. Figure 22 describes the Doppler frequency bin spread on the Y-axis for the DDMs generated by the proposed methodology, where t_{coh} is given by Table 5 and F_{max} is 10 KHz. The bins are spread out decreasing from left to right, and the middle bin represents the zero frequency. In the subsequent sections, the results of each simulated run for each modulation are presented. For comparisons of both methodologies, the peak metrics have been plotted and analyzed. In this section, the acquisition metric is considered as the ratio of the largest and second-largest peak. If the ratio is greater than the threshold, the signal is acquired.

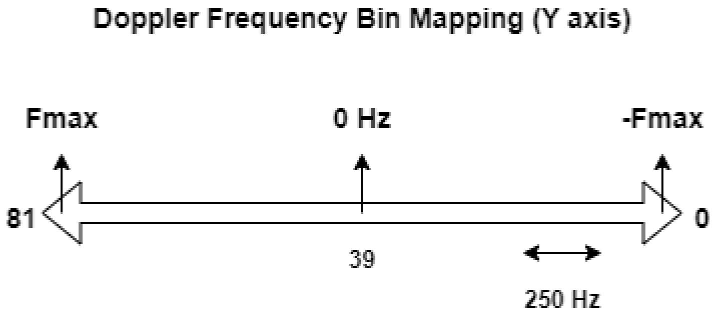

Figure 21. Doppler frequency bin spread of the DDM Y-axis generated for PCPS method.

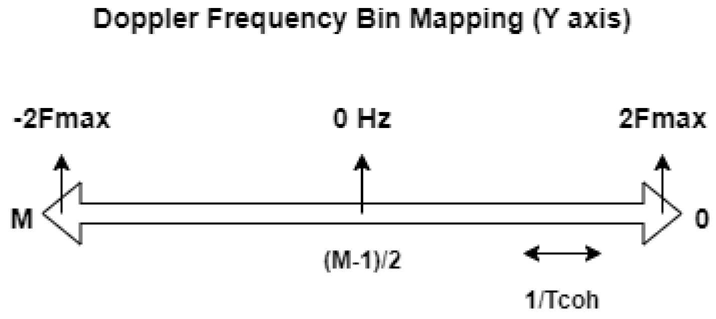

Figure 22. Doppler frequency bin spread of the DDM Y-axis generated for proposed method.

4.2.1 Results of Simulated L1 GPS C/A-code Acquisition

For the first scenario, only the GPS L1 C/A-code modulation was enabled for transmission. During the simulation, the received power was kept at the nominal -128 dBm. All 32 GPS satellites were enabled for transmission. The SimGEN software reported that during the scenario, only satellites 4, 13, 17, 20, and 23 were visible and therefore received by the simulated antenna. The entire 30-second duration of the simulation was captured in a binary file and processed. The acquisition peak metrics are compared in Figure 22. The bars coloured in cyan represent the proposed processing methodology metrics, and the blue bars represent PCPS metrics. For direct signal analysis, the threshold was set at 2.5, as highlighted by the red line, and the metric was defined as the ratio of the two largest peaks.

From Figure 23, both acquisition methods demonstrated equivalent results in acquiring all the satellites. However, for the proposed methodology, the metrics for satellites 4 and 13 are reduced, meaning the ratio of the two peaks was decreased by about 33% when compared to PCPS. The ratio of the peaks was still sufficient to cross the threshold for successful detection. This reduction was primarily due to the performed down-sampling. However, this reduction was also seen in the satellites that were not visible, indicating that the down-sampling had negligible effect on the detection accuracy.

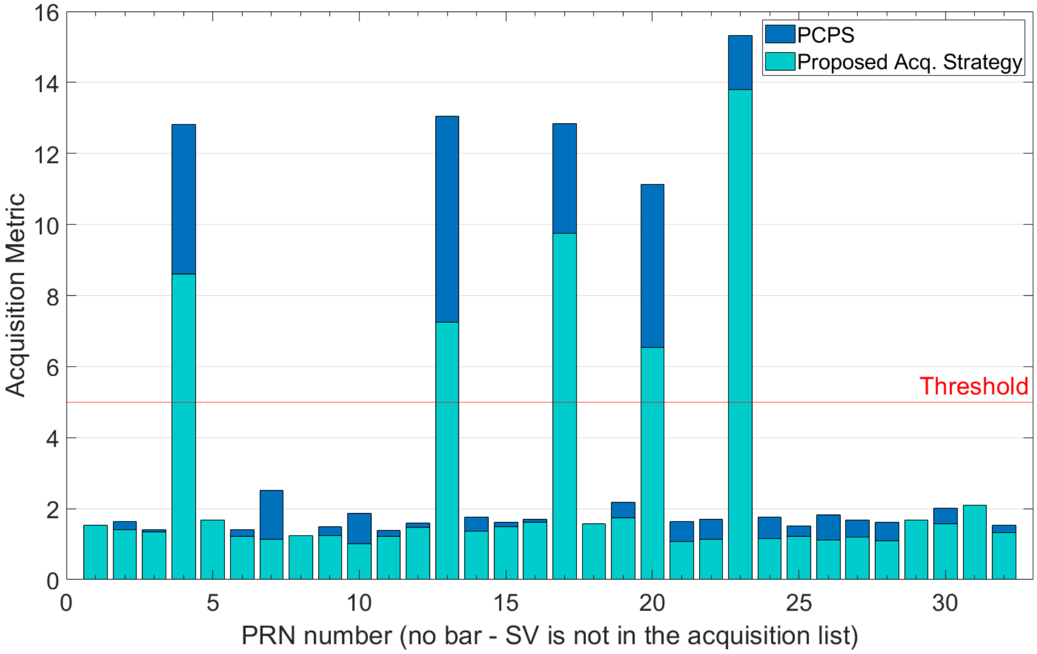

Figure 23. Acquisition metrics for both conventional acquisition of PCPS and proposed acquisition strategy for GPS L1 C/A-code.

The Doppler frequency shift, code delay, and correlation results of the DDM for the acquired satellite 13 for both methods were analyzed next. Figure 24 shows the DDM for satellite 13 generated with the conventional method. The peak is located at a delay of 23901 chips and a frequency bin of 31. As seen in Figure 21, this bin corresponds to a Doppler frequency of -2250 Hz. It can be easily deduced from this search space that the peak correlation magnitude is well above the noise floor, indicating a successful detection.

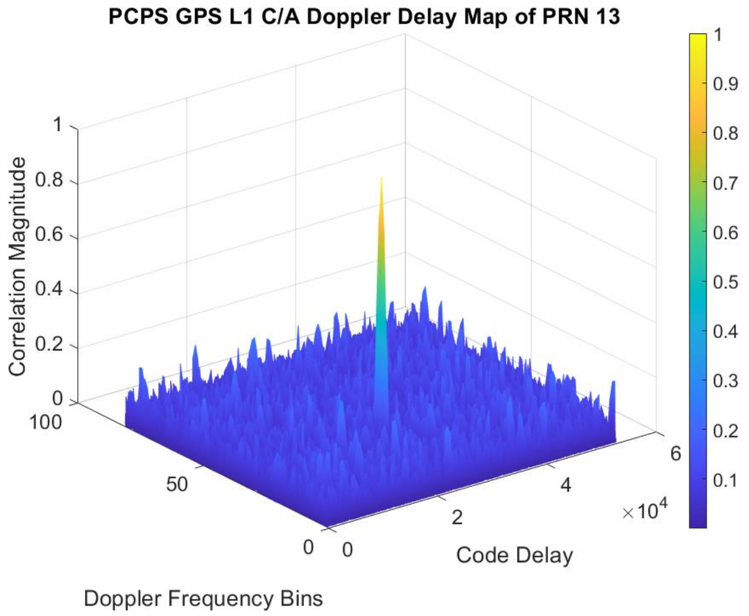

Figure 24. Delay Doppler search field for GPS L1 C/A-code satellite 13, generated from conventional acquisition.

In Figure 25, the DDM generated with the proposed method is shown. The peak is located at the code delay of 1754 and the frequency bin of 41. From Figure 22, the bin translates to a Doppler frequency shift of -2000 Hz. From this result it is deduced that the peak is well above the noise floor, although the correlation magnitude is significantly less when compared to PCPS. This outcome is a result of the smaller FFT transform sizes used for correlation during processing. However, the magnitude in relation to the noise floor remains the same, indicating successful detection.

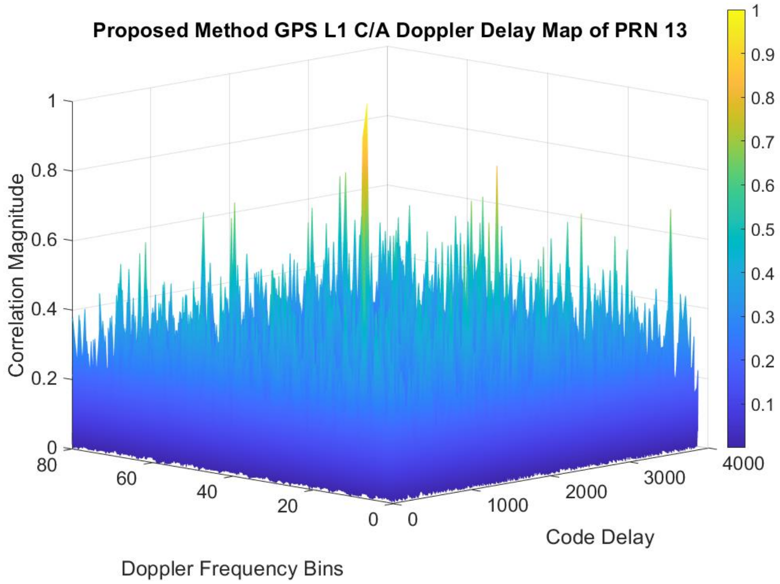

Figure 25. Delay Doppler search field for GPS L1 C/A-code satellite 13 generated from proposed acquisition strategy,

The down-sampled code delay is restored to the original sampling frequency resolution of 53 MHz by multiplying the code delay by the down-sampling factor H. For GPS L1 C/A-code from Table 6, H is 13.64, therefore the recovered delay is 23,914, a difference of 10 samples per code chip between PCPS. The difference that is within the duration of a chip: $\Delta_{chip}=\frac{F_s}{F_{code}}$ since the chip is oversampled the original PRN bit is still found. It is concluded that the proposed acquisition strategy maintains its accuracy in determining the code delay. From the simulation results, PRN 13 was reported to have a Doppler frequency shift of -2152 Hz. The given Doppler from PCPS is -2250 Hz, and for the proposed method is given as -2000 Hz. In Table 8, the execution time is compared for both methods for all modulations when searching through all the visible 32 satellites of the constellation. For searching the GPS L1 C/A modulation, the proposed strategy took an amazing 1.5 seconds to complete the search while PCPS took 41 seconds, equivalent to a 27 times reduction in execution time. Overall, we can conclude that the proposed strategy provides a fast and computationally efficient method for GPS L1 C/A-code acquisition.

Table 8. Execution time comparisons for searching all 32 visible satellites for each modulation between PCPS and proposed method.

Modulation	PCPS execution time (S)	Proposed method execution time (S)	Percentage of execution time over PCPS (%)
GPS L1 C/A	41	1.5	3.65
GPS L2 CM	915	264	28.85
GPS L5 I/Q	21	9	42.85
Galileo E1-B	52	22	42.30

4.2.2 Results of Simulated GPS L2 CM Acquisition

For the second scenario, only the GPS L2 CM modulation was enabled for transmission. During the simulation, the received power was kept to the nominal -131 dBm. All 32 GPS satellites were enabled for transmission. The SimGEN software reported that during the scenario, only satellites 4, 13, 17, 20, and 23 were visible and received by the simulated antenna. The entire 30-second duration of the simulation was captured in a binary file and processed. The acquisition detection performance of both methods was analyzed by comparing the acquisition metrics, which represent the ratio of the two largest peaks within the DDM. The results are shown in Figure 26. The bars coloured in cyan represent the proposed strategy metrics, and the blue bars represent PCPS metrics. For direct signal analysis, the threshold was set at 15, as highlighted by the red line. Successful detection is warranted if the ratio of the two largest peaks crosses the threshold.

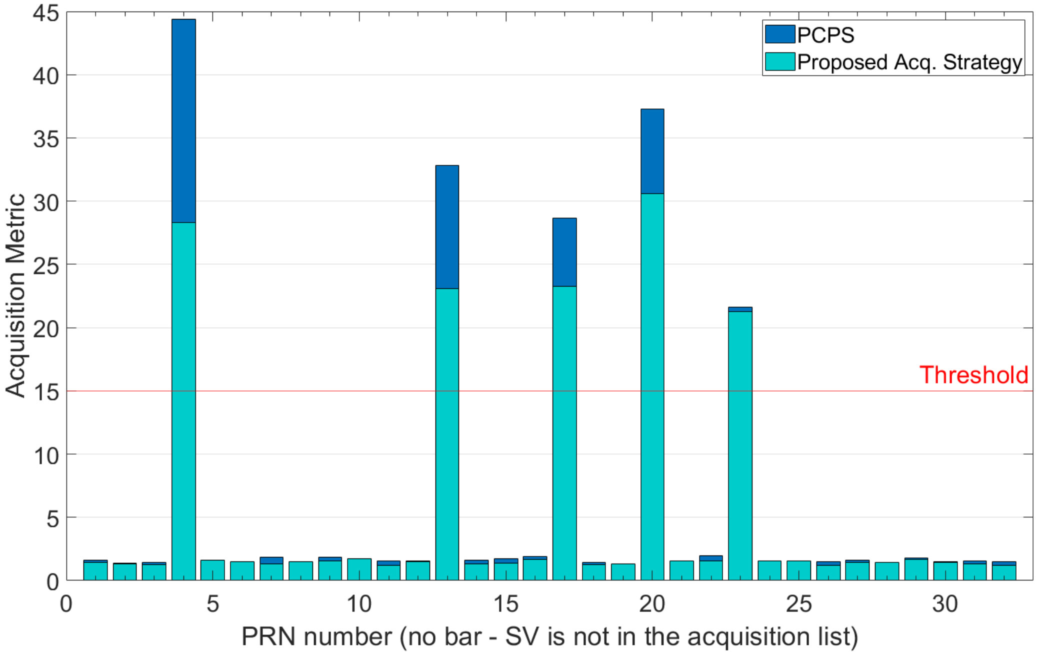

Figure 26. Acquisition metrics for both conventional acquisition of PCPS and proposed acquisition strategy for GPS L2C

From Figure 26, both acquisition methods demonstrated equivalent performance in successfully acquiring all the visible satellites as reported by the simulation. However, for the proposed methods reductions in the peak ratios are seen. Starting with satellite 4, the metric is reduced by about 39%, for satellite 13 this reduction is about 31%, while for satellites 17 and 20 the reduction is about 15%. Overall, the ratio of the peaks is still significant enough to be declared the satellite as detected, again this reduction in the threshold values is due to the resampling of the initial signal sample. Similarly, to GPS L1 C/A-code acquisition metrics an overall reduction of 20% is seen in the ratios of the satellites that are not visible. It can be concluded that detection accuracy of visible satellites of the proposed method is consistent with the conventional PCPS method.

The following Doppler frequency shift, code delay and correlation results are analyzed for the DDM of satellite 13 for both methods. In Figure 27 the DDM of satellite 13 generated with PCPS is shown, the peak is located at the code delay of 450,082 chips in the 32nd frequency bin. For PCPS method the code delay resolution is equivalent to $\Delta t = \frac{1}{F_s}$, while the Doppler frequency resolution is equivalent to 250 Hz, from figure 22 the Doppler frequency estimate is found to be -2000 Hz.

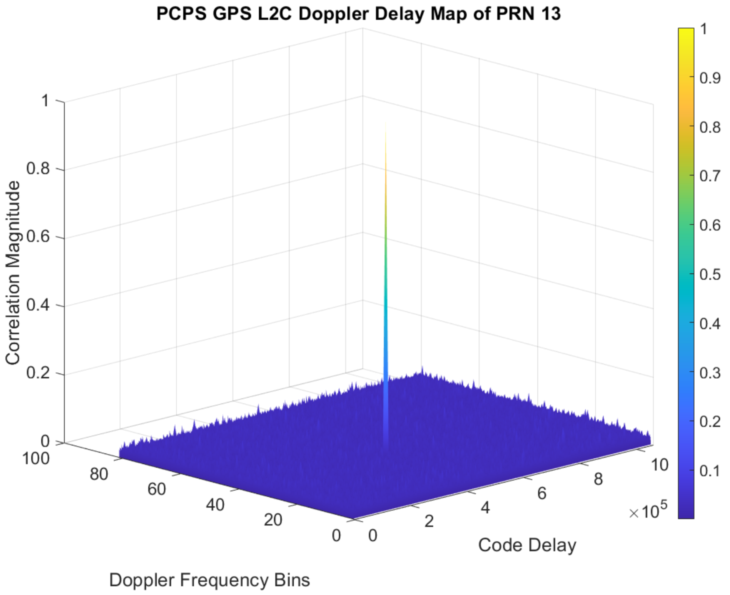

Figure 27. Delay Doppler search field for GPS L2 CM satellite 13 generated from conventional method

In Figure 28, a plot of the DDM of satellite 13 generated with the proposed method is shown. The peak is located at a delay of 35936 chips and in frequency bin 437. The proposed strategy has a code delay resolution of $\Delta t = \frac{1}{F_r}$ and a Doppler frequency resolution of $\frac{1}{t_{coh}}$ resulting in a Doppler frequency resolution of 50 Hz per bin. The proposed method estimated a Doppler frequency of -1850 Hz, while the simulation reported the Doppler frequency shift of PRN 13 to be -1878 Hz. This is due to the increased Doppler frequency resolution resulting from the longer t_{coh} coherent integration time of 20 ms. The peak correlation magnitude for the proposed method is lower than PCPS, which is a result of the shorter FFT sample size during correlation.

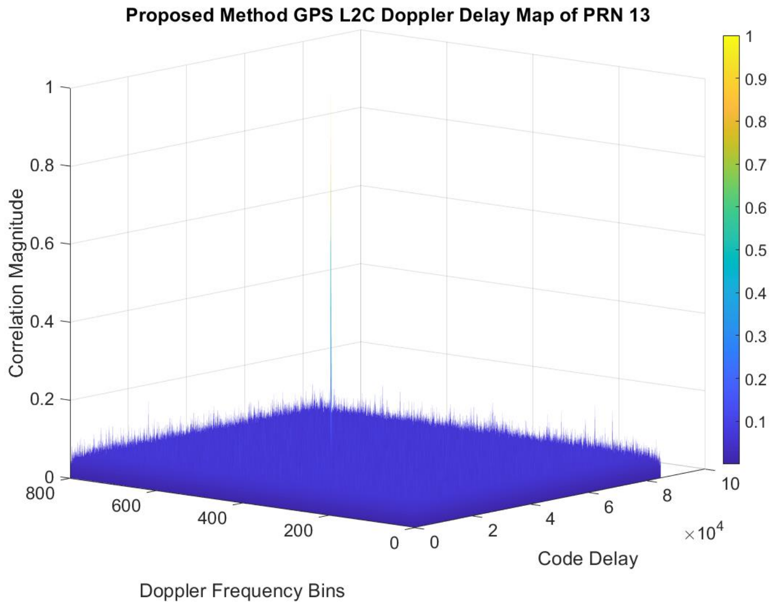

Figure 28. Delay Doppler search field for GPS L2 CM satellite 13 generated from proposed acquisition strategy

The code delay resolution can be recovered to the original sampling frequency by multiplying by the resampling factor H. For GPS L2C from Table 7, H is 12.5. The recovered delay is 450,111, which is a difference of 29 samples per code chip compared to PCPS. This difference is caused by rounding that occurs during resampling. However, the difference is within the duration of a code chip $\Delta_{chip}=\frac{F_s}{F_{code}}$, with a code frequency of $F_{code} = 1.023\ \mathrm{MHz}$ and a sample frequency of $F_s = 53\ \mathrm{MHz}$ for GPS L2C results in 53 samples per chip. The code delay estimation between the proposed method and PCPS is approximately half of the chip's sample duration, therefore the proposed methodology maintains the precision of the code delay estimate despite the lower sample size.

The proposed strategy for GPS L2C signal acquisition demonstrates improved efficiency and precision compared to the conventional PCPS method. The execution time for the proposed method was 3 times faster, taking only 264 seconds compared to PCPS's 915 seconds. This performance gain is attributed to the reduction in the required FFT transform size from 1,060,000 for PCPS to 1024 for the proposed method. Additionally, the proposed method's Doppler frequency resolution of 50 Hz results in a more precise estimation of the Doppler shift. Overall, the proposed strategy is a computationally efficient and accurate solution for GPS L2C signal acquisition.

4.2.3 Results of Simulated L5 GPS I/Q acquisition

In figure 29, the acquisition performance of the proposed and conventional methods is compared using peak metrics for the GPS L5 I/Q modulation. The simulation was conducted using only satellites 1, 4, 11, 13, 17, 20, 23, 25, and 31, which were visible during the simulation. The threshold for successful detection was set at 2, as indicated by the red line. Both methods were able to acquire all visible satellites with equivalent performance. However, the metrics for the proposed method showed a 50% reduction for satellites 1 and 31, and a 20% reduction for satellites 11, 13, and 17. This reduction is likely due to the down-sampling that occurred during the proposed method. Despite the reduction, the metrics are still greater than the threshold and all the satellites were still detected. The minimum bandwidth for GPS L5 I/Q is 20.46 MHz, resulting in a minimum sampling frequency of 40.92 MHz. This modulation appears to be less susceptible to resampling with a resampling factor of 1.11. Overall, the proposed method still maintains accuracy in detecting all visible satellites, even with sub-optimal down-sampling.

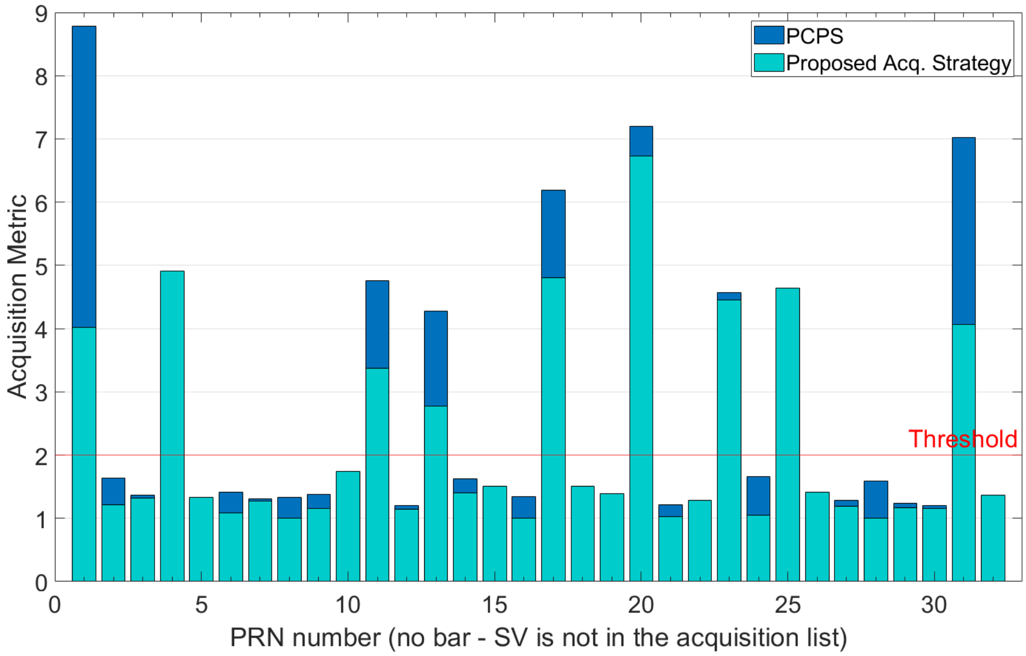

Figure 29. Acquisition metrics for both conventional acquisition of PCPS and proposed acquisition strategy for GPS L5 I/Q.

Figure 30 shows the DDM generated for satellite 13 using the PCPS method. The peak is located at a code delay of 37141 chips and a frequency bin of 33. The DDM has a code delay resolution of $\Delta t = \frac{1}{F_s}$ and a Doppler frequency resolution of 250 Hz. The estimated Doppler shift is -2000 Hz, indicating a clear detection above the noise floor.

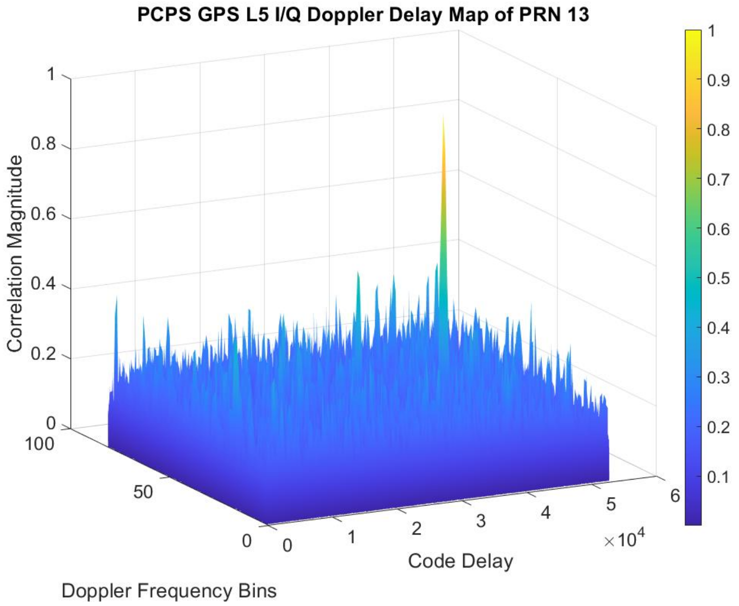

Figure 30. Delay Doppler search field for GPS L5 I/Q satellite 13 generated from conventional method.

In Figure 31, a plot of the DDM of satellite 13 generated with the proposed acquisition method is shown. The peak is located at the delay of 33337 chips within the 41st frequency bin. For the proposed method, the code delay resolution is $\Delta t = \frac{1}{F_r}$ and the Doppler frequency resolution is $\frac{1}{t_{coh}}$, which for GPS L5 I/Q results in a resolution of 1000 Hz.

From Figure 22, the Doppler frequency bin translates to a Doppler frequency shift estimate of -2000 Hz. The simulation reported that the Doppler frequency shift of PRN 13 was -2050 Hz, and both methods derived an accurate Doppler frequency estimate given their respective frequency resolutions. As in previous analyses, the code delay can be recovered by multiplying by the resampling factor H. For GPS L5I/Q, from Table 7, H is 1.114, therefore the recovered delay is 37,138, a difference of 3 samples per code chip between PCPS and the proposed method. The code frequency of GPS L5 I/Q is 10.23 MHz, resulting in a code chip duration of 5 samples. Given that the difference is within the duration of a chip, the correct delay can still be extracted. The difference is a result of rounding that occurred during resampling. Overall, even with the sub-optimal down sampling, the correct code delay was estimated by the proposed acquisition method.

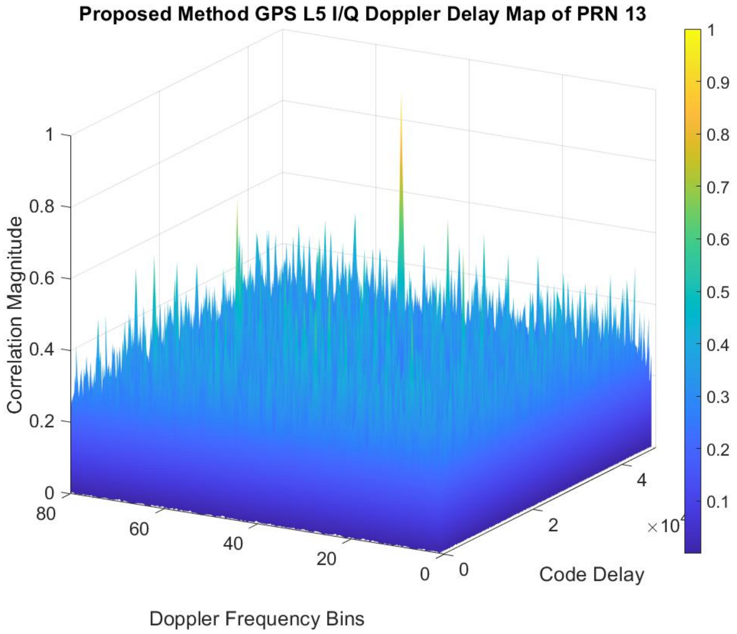

Figure 31. Delay Doppler search field for GPS L5 I/Q satellite 13 generated from proposed method.

Table 8 shows a comparison of the execution time for both methods when searching through all 32 visible GPS L5 I/Q satellites. The proposed strategy took 9 seconds to complete the search, while PCPS took 21 seconds, resulting in a 2-times reduction in execution time. Despite the sub-optimal resampling factor of 1.114, the proposed strategy still accurately detected the visible satellites. The proposed strategy utilizes a smaller FFT transform size of 2738, compared to PCPS's 53,000, making it an efficient method for acquiring the GPS L5 I/Q modulation.

4.2.4 Results for Simulated Galileo E1-B

In Figure 32, the results of the proposed and conventional acquisition methods when analyzing the Galileo E1-B modulation are shown. The simulation indicated that only satellites 6, 7, 8, 9, 12, 13, 14, 15, 19, 20, and 21 were visible and received by the simulated antenna. The performance of both methods was evaluated by comparing the ratio of the two largest peaks within the DDM, with a threshold of 2 for successful detection. The proposed method results in a 50% reduction in peak ratios compared to the conventional method, while still maintaining sufficient metrics to detect all visible satellites. This reduction is due to the use of band-pass filtering and resampling in the proposed method.

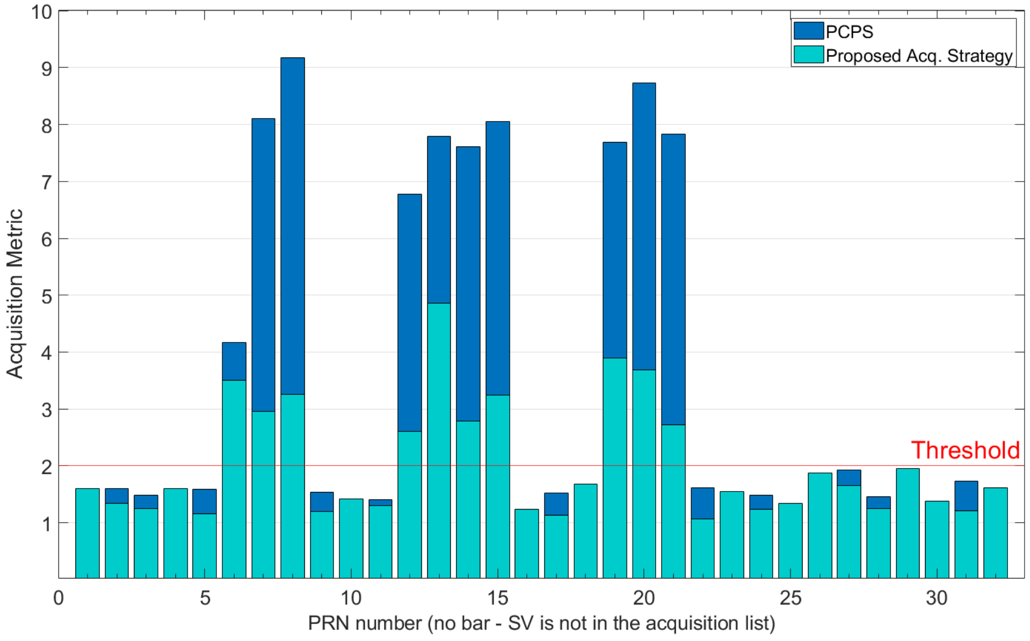

Figure 32. Acquisition metrics for both conventional acquisition of PCPS and proposed acquisition strategy for Galileo E1-B.

In Figure 33, a plot of the DDM for satellite 6 generated with the conventional PCPS method is shown. The peak is located at a delay of 183,775 chips and in the 32nd frequency bin, which translates to a Doppler frequency shift of -2250 Hz according to Figure 21. The peak is clearly visible above the noise floor, indicating a successful detection of satellite 6.

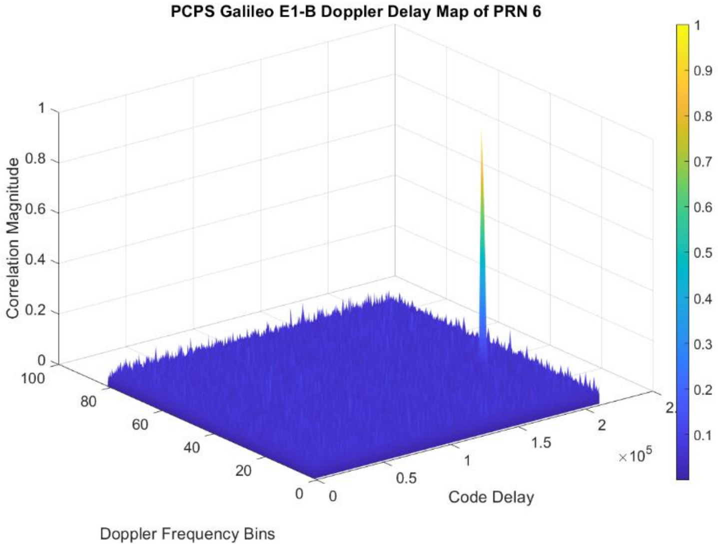

Figure 33. Delay Doppler search field for satellite 6 for the conventional method for Galileo E1-B.

In Figure 34, a plot of the 2-dimensional space of satellite 6 generated with the proposed acquisition strategy is shown. The peak is located at a delay of 28894 chips and in the 153rd frequency bin. The proposed strategy has a code delay resolution of $\Delta t = \frac{1}{F_r}$ and a Doppler frequency resolution of $\frac{1}{t_{coh}}$, with a coherent integration time of 4 milliseconds for Galileo E1-B, resulting in a frequency resolution of 250 Hz. The frequency bin translates to a Doppler frequency shift estimate of -2250 Hz according to Figure 22. The simulation reported a Doppler frequency shift of 2354 Hz, both methods derived accurate Doppler frequency shift estimates given their respective frequency resolutions. The resampling factor H for Galileo E1-B is 6.36, resulting in a recovered delay of 183,765, with a difference of 9 chips per sample between PCPS. The Galileo E1-B data channel has a code frequency of 4.092 MHz, resulting in a samples per chip of 13 with a sample frequency of 53 MHz. The overall difference of 9 chips is slightly more than half of a chip, but still within a chip duration. The loss in precision is again due to rounding during resampling of the signal.

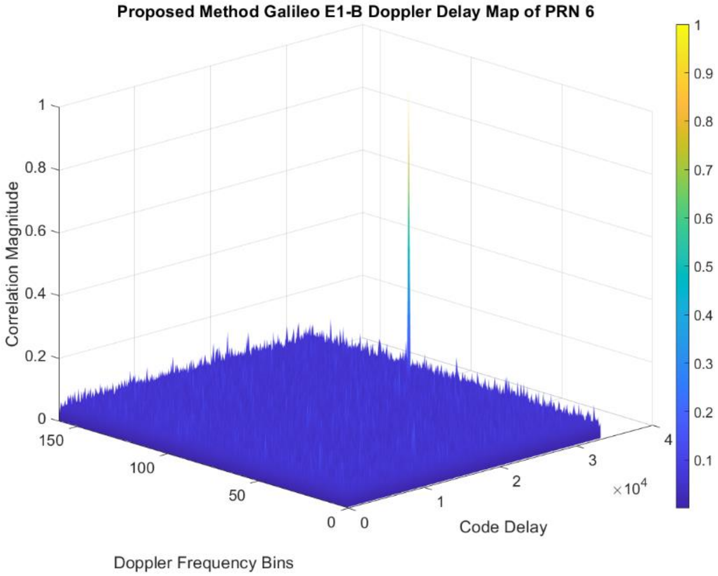

Figure 34. Delay Doppler search field for satellite 6 for the proposed acquisition strategy for Galileo E1-B.

The proposed strategy took 22 seconds to complete the search, while PCPS took 52 seconds, resulting in a roughly 2 times reduction in execution time. Additionally, the proposed strategy required a maximum FFT transform size of 418, while PCPS acquisition required an FFT transform size of 212,000, a significantly larger size. Given that both methods returned the correct acquisition, it can be concluded that the proposed strategy was able to accomplish this at half the execution time of PCPS. Overall, taking into consideration all factors, the proposed acquisition strategy proved to be an efficient method for acquiring the Galileo E1-B modulation.

In conclusion, the results of the proposed method were consistent with the conventional method of PCPS. Setting the threshold to the ratio of the two largest peaks to be the peak metrics has proven to be beneficial. For one, the ratio creates a normalized acquisition metric regardless of the correlation magnitudes. Secondary, if there exists more than one peak that crosses the conventional threshold the ratio would serve as a constant correlation magnitude. Both methods acquired the same satellites and code delay, additionally both methods had precise estimations of the Doppler frequency shift; however, the proposed method derived the estimations with reduced execution time and FFT transform size when compared to the conventional method of PCPS.

4.3 Weak Signal Acquisition Analysis

In this work, weak signals are defined as signals with reduced signal strength below their nominal received power, as described in Table 7. To generate reflectometry observables, the payload's nadir antenna would receive reflected signals from the surface, and the process of reflection attenuates the signal strength below the nominal power. For this reason, this analysis helps to serve as an estimation of the proposed method's acquisition performance when considering reflectometry observables.

For weak signal analysis, additional non-coherent integration over multiple code periods is performed, represented by variable K in Equation 33. By non-coherently integrating multiple code periods, the signal-to-noise ratio is improved, increasing the probability of detecting a weak signal (Borio et al. 2008). The number of periods to integrate over, K, is derived from Equation 42 by additionally deriving the non-centrality parameter λ for a chosen probability of detection and false alarm. For this work and analysis, the probability of detection P_d was set to 0.9 and the probability of false alarm P_f set to 0.001 for all the examined modulations.

The received carrier-to-noise power density, also known as the carrier-to-noise ratio (C/N_0), is expressed in dB-Hz. In this work and analysis, the noise power density N_0 is assumed to be thermal noise at the common value of 290 K or 15° Celsius. From Equation 42, the thermal noise density is derived to be -174 dBm/Hz. Therefore, the C/N_0 can be found by subtracting the thermal noise N_0 from the received power of the signal.

$$\begin{cases} N_0 = 10\,log(kT) \\ k = 1.38 * 10^{-23} \\ \quad T = 290K \end{cases} \qquad \text{Equation 42.}$$

In this thesis, the value of C/N_0 was constrained to 35 dB-hz. To determine the number of non-coherent integrations needed to achieve a 90% probability of detection for a C/N_0 of 35 dB-Hz for each modulation, Equation 40 was utilized. As the parameter λ is dependent on the Doppler frequency shift f_d, the global average probability was evaluated for each Doppler frequency bin. The averaging was performed for each modulation, and the non-coherent integration value K was set to range from 0 to 40. Table 9 shows the number of non-coherent integrations required for each modulation to reach a probability of detection of 90% for a C/N_0 of 35 dB-hz.

Table 9. Number of non-coherent integrations required for each modulation to reach a probability of detection of 90% for a C/N_0 of 35 dB-hz.

Modulation	**Number of non-coherent integrations $\mathbf{K}$**
GPS L1 C/A-code	15
GPS L2C	5
GPS L5 I/Q	10
Galileo E1-B	30

To verify the theoretical performance of the proposed acquisition strategy, extensive Monte Carlo simulations were performed using the GSS9000 simulator. Multiple scenarios were simulated, in which the received power of the simulated antenna was reduced by 1 dBm for a total of 20 scenarios for each modulation, starting from their nominal power. Each scenario ran for 30 seconds and was captured by the NT1065 front-end. For each of the four modulations, the data files consisted of raw simulated data ranging from a C/N_0 of 26 to 46 dB-Hz, totaling to 20 data sets for each modulation. For each data file, 300 acquisitions using the proposed strategy were performed and analyzed, each acquisition begins by reading a random location in the file. From the results of the 300 acquired acquisitions, the number of detected satellites was recorded. If the number of satellites was equivalent to what was received by the simulated antenna as reported by SimGEN, the acquisition was confirmed as successful. The probability of detection for the carrier-to-noise density was the average of the 300 detection trials. The trials were run three times and averaged and plotted in a figure. In total, 900 simulations were performed to generate a large enough sample to derive the mean probability of detection for each C/N_0 given a number of non-coherent integrations.

The results of the Monte Carlo simulations for each modulation are shown in Figure 35. The probability of detection is plotted as a function of the carrier-to-noise ratios. Starting with the GPS L1 C/A-code modulation, the in-coherent integration value, K, is 15. At a C/N_0 of 35 dB-Hz, the probability of detection was indeed 90%, demonstrating a match between the theoretical performance calculations and the results obtained from the Monte-Carlo trials. Afterwards, the probability of detection drops significantly with each decrease in carrier-to-noise ratio, as expected. It can be concluded that the proposed acquisition strategy maintains sensitivity to weakened GPS L1 C/A signals.

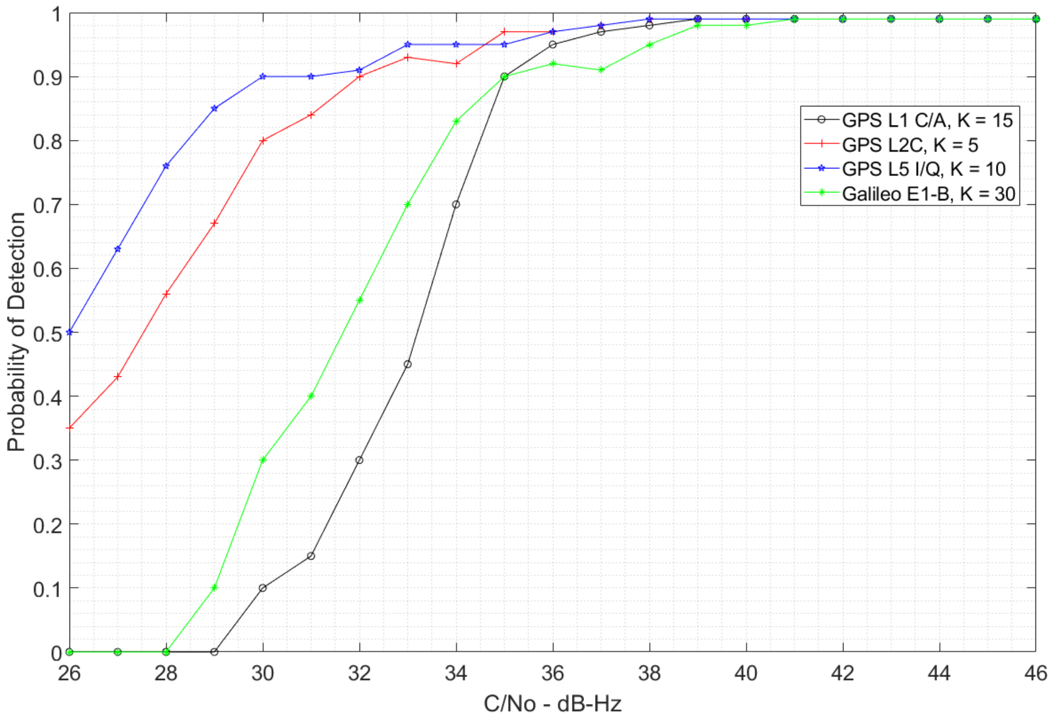

Figure 35. Carrier-to-Noise density versus probability of detection for given value of in-coherent integrations K, for each modulation.

For Galileo E1-B, the in-coherent integration value K was 30, and at a C/N_0 of 35 dB-Hz, the probability of detection was 0.9. However, unlike GPS L1 C/A-code, the probability of detection rapidly decreases. The decrease can be attributed to the fact that the Galileo E1-B signal is intermixed with its pilot component E1-C. As a result, by demodulating only the data channel E1-B, only 66% of the total signal strength is received, as shown in equation 12. However, this loss in sensitivity is offset by the significant reduction of the FFT transform size. Additionally, sensitivity can be increased by demodulating and acquiring the E1-C pilot signal and combining the correlation results coherently. Furthermore, the number of in-coherent integrations can also be further increased for enhanced sensitivity.

For GPS L2C modulation, the in-coherent integration value K was 5, and at a C/N_0 of 35 dB-Hz, the proposed method had a higher sensitivity than theoretically expected. The probability of detection was expected to be 0.9 at a C/N_0 of 35 dB-Hz, but it was a higher value of 0.95. Additionally, at a C/N_0 of 32 dB-Hz, the probability of detection was equivalent to 0.9. The improved performance can be attributed to the much longer code period of 20 milliseconds, as more data is correlated, resulting in improved robustness to signal attenuation. The longer coherent integration period is a key improvement introduced by the GPS L2C modulation, which enhances weak signal reception.

Finally, the in-coherent integration value K for GPS L5 I/Q was determined to be 10 for a C/N_0 of 35 dB-Hz. The results of the simulation showed that the proposed acquisition strategy had higher sensitivity than what was theorized. At a C/N_0 of 35 dB-Hz, the probability of detection was found to be 0.95, which is higher than expected. Additionally, at a C/N_0 of 26 dB-Hz, the probability of detection was found to be 0.5, indicating that the proposed method remains sensitive to weakened signals. The increased sensitivity to weakened signal can be attributed to the large bandwidth of the GPS L5 I/Q signal, which is 10 times greater than GPS L1 C/A or GPS L2C. The larger bandwidth makes the transmitted signal more robust to attenuation. The increased signal bandwidth is a key enhancement of GPS L5 I/Q modulation, particularly for safety-of-life applications.

In conclusion, the proposed acquisition method for GPS and Galileo signals has been shown to be highly efficient and accurate in acquiring weak signals. The method utilizes a peak ratio threshold as a metric for direct acquisition and has been shown to be consistent with the conventional method of PCPS. Additionally, the proposed method has been shown to have a significant reduction in execution time and FFT transform size when compared to the conventional method. The results of the Monte Carlo simulations have further reinforced the efficiency of the proposed method, as it maintains good sensitivity with the benefit of reduced computational costs for all the examined modulations. Overall, the proposed method is a reliable and efficient solution for acquiring weak signals in navigation satellite systems.

Chapter 5: Conclusion and Recommendations

In this chapter, the proposed acquisition methodology is discussed, and a comprehensive summary of its results is presented. A comparison between the proposed methodology and the conventional method is made, with a focus on performance difference regarding execution time. The following section draws further conclusions from the analysis and provides recommendations for future work.

5.1 Conclusions

5.1.1 Developed Acquisition Process

The developed acquisition process represents a novel approach that combines two established methodologies for efficient GNSS acquisition. The initial resampling process is employed to reduce the overall data size required for acquisition prior to applying correlation filters, resulting in a significant reduction in memory requirements for digital signal processing. Additionally, the implementation of partial correlation reduces the necessary FFT computations, further streamlining the acquisition process. By utilizing less memory and computational power, the proposed methodology achieves comparable acquisition performance to conventional methods. The reduction in memory cost can also be leveraged to improve weak signal sensitivity through in-coherent integration, making it possible to receive weakened GNSS signals. Overall, these advancements make the proposed acquisition process a highly efficient and promising solution for GNSS acquisition.

5.1.2 Results

The proposed method, based on a peak-to-peak ratio threshold, was able to successfully acquire the GPS L1 C/A-code, L2 CM, L5 I/Q and Galileo E1-B modulations. The method also showed a significant reduction in execution time and FFT transform size when compared to PCPS. Additionally, the proposed method was able to maintain good sensitivity for weak signals, making it suitable for applications such as reflectometry observables.

The proposed method is optimized for use with modern broadband GNSS front-end receivers and was able to acquire all modulations with the same accuracy as the conventional method while requiring significantly less FFT transform size, with a reduction of 1035 times for the demanding GPS L2C modulation, and of 227 times for GPS L1 C/A-code. The implementation and subsequent execution were done using MATLAB, resulting in a 3 times average reduction in execution time when compared to the conventional method, with the greatest reduction of 27 times observed for GPS L1 C/A-code acquisition. Furthermore, the proposed strategy offers enhanced sensitivity to weakened signals by incorporating appropriate non-coherent integration, despite reducing the nominal transmit power by 10 dB. This was accomplished while utilizing less data in the processing stage. The reduced acquisition time provided by the proposed process offers a higher refresh rate for repetitive GNSS-R measurements, as well as faster acquisition time, resulting in a quicker coarse observable. Resulting in reduced time for GNSS signal acquisition and subsequent tracking.

5.2 Future Work

This section delves into potential areas for further improvement of the proposed acquisition process. Specifically, the discussion focuses on future work that can enhance the overall application of the proposed acquisition strategy, including considerations for real-time processing hardware, sensitivity improvements, and verification of acquisition sensitivity in real-world scenarios. Addressing these areas has the potential to further optimize the proposed acquisition process for improved performance and reliability in practical applications.

5.2.1 Impact of additional modulation acquisition

This research presents evidence that a combination of pre-acquisition processing and partial correlation can be an effective approach for implementing an acquisition strategy in software defined GNSS receivers. However, it should be noted that this study only examined four modulations: GPS L1 C/A-code, L2C, L5 I/Q, and Galileo E1-B. With the advent of modernized GPS L1C and Galileo E5 and E6 modulations, soon to be available for civilian use, this research offers only a glimpse of the full potential of this approach. Additionally, the NT1065 front-end has the capability to simultaneously receive signals from other GNSS constellations such as GLONASS, IRNSS, and BeiDou (NTLab, 2016). Therefore, this study only examines the strategy on a small subset of the available GNSS signal spectrum. Expanding the proposed acquisition strategy to other GNSS modulations would significantly increase the number of observable signals for the payload, providing enhanced global coverage by including regional-based systems, redundant observations, and a larger set of reflectometry data. It would be beneficial to further explore this system and its potential to take advantage of the entire public GNSS network.

5.2.2 Impact on Hardware Considerations

Additionally, the proposed strategy is a good candidate for implementation on low-cost digital platforms with very limited processing resources. For example, the Zynq-7010 FPGA board contains 1.8 MB of on-board FPGA memory blocks and 66 digital signal processing elements such as multipliers and adders. These components are packaged together with a dual-core ARM processor (Crockett et al 2017). The platform is typically available for $149. Furthermore, FPGAs have the capability to accelerate FFT calculations significantly when compared to a standalone computer (Varma et al 2013). Due to the reduction in computational complexity and lower costs associated with smaller integrated components, the proposed strategy is well-suited for low-end FPGA devices. Implementing the processing on FPGA is ideal as it can take advantage of the flexible nature of the FPGA to realize a fully reconfigurable SDR. To take advantage of these features the future work involves implementing this strategy on a low-cost FPGA platform like the Zynq-7010 for future field campaigns. However, this task is technically challenging, the FPGA board will require additional programming of dedicated firmware to operate the underlying hardware to realize a fully enclosed system further verification, synthesis, and functional verification needs to be performed. Furthermore, specific logic and functions may need to be built from scratch if vendor templates are not available. Overall, it would be interesting to see this highly efficient GNSS acquisition method fully integrated with a low-cost platform to achieve an efficient and cost-effective GNSS receiver design.

5.2.3 Sensitivity improvement

In this research, the focus was on acquiring and analyzing the data component of each modulation. However, it is worth noting that GPS L2C, GPS L5 I/Q, and Galileo E1-B also include a parallel pilot component transmitted alongside the data component. By solely examining the data modulation and disregarding the pilot component, the acquisition sensitivity was reduced. To enhance the sensitivity of the method, it would be beneficial to incorporate the pilot component into the analysis. Additionally, optimizing the threshold value to better align with the desired detection probability can further improve the acquisition strategy. While signals attenuated by 10 dBm were analyzed in this work, it would be valuable to investigate the strategy's performance with signals attenuated by more than 10 dBm and determine the required number of in-coherent integrations for signal detection. Previous studies, such as the work by Borio et al. (2008), have explored the acquisition of Galileo E1-OS by coherently combining both the pilot and data signals. Future research could explore integrating such coherent combination methodologies with pilot signal acquisition to enhance sensitivity performance.

5.2.4 Real-data processing and verification

This thesis tested the proposed acquisition process using simulated data sets and verified its effectiveness through Monte-Carlo simulations with a simulated receiving GNSS antenna. However, to fully understand the proposed strategy's potential in real-world scenarios with real GNSS antennas, it is necessary to conduct field-based data acquisition of weak GNSS signals and characterize them. This task is not without its challenges, as it requires in-field spectrum analysis tools to identify and characterize a weak GNSS signal. Nonetheless, pursuing this research is crucial for characterizing the performance of the proposed acquisition process. This work would help determine the efficacy of proposed acquisition process for GNSS signal acquisition and application of the process for GNSS-R measurement retrieval.

References

Ávila Rodríguez, J. Á. (2008). *On generalized signal waveforms for satellite navigation* (Doctoral dissertation, München, Univ. der Bundeswehr, Diss., 2008).

Bastide, F., Akos, D., Macabiau, C., and Roturier, B. (2003, September). Automatic gain control (AGC) as an interference assessment tool. In *Proceedings of the 16th International Technical Meeting of the Satellite Division of The Institute of Navigation (ION GPS/GNSS 2003)* (pp. 2042-2053).

Borio, D. (2008). *A statistical theory for GNSS signal acquisition*. PHD Dissertation Polytecnico di Torino.

Borio, D., and Presti, L. L. (2008). Data and pilot combining for composite GNSS signal acquisition. International Journal of Navigation and Observation, 2008.

Borre, K. (2006, August). The Galileo signals with emphasis on L1 OS. In *2006 12th International Power Electronics and Motion Control Conference* (pp. 2025-2030). IEEE.

Borre, K., Akos, D. M., Bertelsen, N., Rinder, P., and Jensen, S. H. (2007). *A software-defined GPS and Galileo receiver: a single-frequency approach*. Springer Science and Business Media.

Buist, P. J., and Vollmuller, G. J. (2013, January). Onboard FFT Data Processing for GNSS Reflectometry. In *Proceedings of the 2013 International Technical Meeting of The Institute of Navigation* pp. 597-603.

Camps, A., Park, H., Castellví, J., Corbera, J., and Ascaso, E. (2020). Single-pass soil moisture retrievals using GNSS-R: Lessons learned. *Remote Sensing*, *12*(12), 2064.

Caparrini, M., Egido, A., Soulat, F., Germain, O., Farres, E., Dunne, S., and Ruffini, G. (2007, July). Oceanpal®: Monitoring sea state with a GNSS-R coastal instrument. In *2007 IEEE International Geoscience and Remote Sensing Symposium* pp. 5080-5083.

Chew, C., Small, E. E., and Larson, K. M. (2016). An algorithm for soil moisture estimation using GPS-interferometric reflectometry for bare and vegetated soil. *GPS solutions*, *20*(3), 525-537.

Clarizia, M. P., Gommenginger, C., Gleason, S., Galdi, C., and Unwin, M. (2008, July). Global navigation satellite system-reflectometry (GNSS-R) from the UK-DMC satellite for remote sensing of the ocean surface. In *IGARSS 2008-2008 IEEE International Geoscience and Remote Sensing Symposium* (Vol. 1, pp. I-276).

Crockett, L. H., Elliot, R. A., Enderwitz, M. A., and Stewart, R. W. (2014). *The Zynq book: embedded processing with the ARM Cortex-A9 on the Xilinx Zynq-7000 all programmable SoC*. Strathclyde Academic Media.

Edokossi, K., Calabia, A., Jin, S., and Molina, I. (2020). GNSS-reflectometry and remote sensing of soil moisture: A review of measurement techniques, methods, and applications. *Remote Sensing*, *12*(4), 614.

Egido, A. E. (2014). *GNSS reflectometry for land remote sensing applications.* Doctoral dissertation, Universitat Politècnica de Catalunya

ESA, O. (2022). European GNSS (Galileo) open service. *Signal in space. Interface control document. Issue*, *2.0*.

Esterhuizen, S. (2006). *The design, construction, and testing of a modular GPS bistatic radar software receiver for small platforms.* Doctoral dissertation, University of Colorado at Boulder.

Fontana, R. D., Cheung, W., Novak, P. M., and Stansell, T. A. (2001, September). The new L2 civil signal. In *Proceedings of the 14th International Technical Meeting of the Satellite Division of The Institute of Navigation (ION GPS 2001)* pp. 617-631.

Foucras, M., Julien, O., Macabiau, C., and Ekambi, B. (2012, September). A novel computationally efficient Galileo E1 OS acquisition method for GNSS software receiver. In *Proceedings of the 25th International Technical Meeting of the Satellite Division of the Institute of Navigation (ION GNSS 2012)* pp. 365-383.

Foucras, M., Julien, O., Macabiau, C., and Ekambi, B. (2013, April). An efficient strategy for the acquisition of weak Galileo E1 OS signals. In *ENC 2013, European Navigation Conference*

Gleason, S., Gebre-Egziabher, D., and Egziabher, D. G. (2009). GNSS applications and methods.

Hegarty, C. (2003). Alternative Bi-phase GNSS Modulations. *MITRE Memorandum F82-M04-004, The MITRE Corporation, Bedford, Massachusetts*, *24*.

Imam, R., Pini, M., Marucco, G., Dominici, F., and Dovis, F. (2019). UAV-based GNSS-R for water detection as a support to flood monitoring operations: A feasibility study. *Applied Sciences*, *10*(1), 210.

Jia, Y., and Savi, P. (2016, July). Polarimetric GNSS-R measurements for soil moisture and vegetation sensing. In *2016 IEEE International Geoscience and Remote Sensing Symposium (IGARSS)* pp. 5260-5263.

Jia, Y., Savi, P., Canone, D., and Notarpietro, R. (2016). Estimation of surface characteristics using GNSS LH-reflected signals: Land versus water. *IEEE Journal of Selected Topics in Applied Earth Observations and Remote Sensing*, *9*(10), 4752-4758.

Kaplan, E. D., and Hegarty, C. (Eds.). (2017). *Understanding GPS/GNSS: Principles and applications*. Artech house.

Krumvieda, K., Madhani, P., Cloman, C., Olson, E., Thomas, J., Axelrad, P., and Kober, W. (2001, September). A complete IF software GPS receiver: A tutorial about the details.

In *Proceedings of the 14th International Technical Meeting of the Satellite Division of The Institute of Navigation (ION GPS 2001)* pp. 789-829.

Navstar (2021) IS-GPS-705H GPS Space Segment/User Segment L5 Interfaces. Tech. rep., Global Positioning System Directorate Systems Engineering and Integration

Li, C., and Huang, W. (2014). An algorithm for sea-surface wind field retrieval from GNSS-R delay-Doppler map. *IEEE Geoscience and Remote Sensing Letters*, *11*(12), 2110-2114.

Lin, D. M., Tsui, J. B., and Howell, D. (1999, September). Direct P (Y)-Code Acquisition Algorithm forSoftware GPS Receivers. In *Proceedings of the 12th International Technical Meeting of the Satellite Division of The Institute of Navigation (ION GPS 1999)* pp. 363-368.

Marchan-Hernandez, J. F., Camps, A., Rodriguez-Alvarez, N., Bosch-Lluis, X., Ramos-Perez, I., and Valencia, E. (2008). PAU/GNSS-R: Implementation, performance and first results of a real-time Delay-Doppler map reflectometer using global navigation satellite system signals. *Sensors*, *8*(5), 3005-3019.

Martín, A., Ibáñez, S., Baixauli, C., Blanc, S., and Anquela, A. B. (2020). Multi-constellation GNSS interferometric reflectometry with mass-market sensors as a solution for soil moisture monitoring. *Hydrology and Earth System Sciences*, *24*(7), 3573-3582.

Masters, D., Zavorotny, V., Katzberg, S., and Emery, W. (2000, July). GPS signal scattering from land for moisture content determination. In *IGARSS 2000. IEEE 2000 International Geoscience and Remote Sensing Symposium. Taking the Pulse of the Planet: The Role of Remote Sensing in Managing the Environment. Proceedings (Cat. No. 00CH37120)* Vol. 7, pp. 3090-3092. IEEE.

Mitola, J. (1993). Software radios: Survey, critical evaluation, and future directions. *IEEE Aerospace and Electronic Systems Magazine*, *8*(4), 25-36.

Navstar, (2013) G. P. S. "Space Segment/Navigation User Interfaces. Interface Specification IS-GPS-200H."

NTLAB. (2016). NT1065-USB3-Documentation (1.41) [Data sheet]. https://ntlab.lt/product/nt1065_usb3-evaluation-kit/ Accessed (2021).

NTLAB. (2017). NT1065-FMC2-Documentation (3.10) [Data sheet]. https://ntlab.lt/product/nt1065_fmc2-evaluation-kit/ Accessed (2021).

Oppenheim, A. V. (1999). *Discrete-time signal processing*. Pearson Education India.

Ouimet, F., and Tolosana-Delgado, R. (2022). Asymptotic properties of Dirichlet kernel density estimators. *Journal of Multivariate Analysis*, *187*, 104832.

Park, H., Pascual, D., Camps, A., Martin, F., Alonso-Arroyo, A., and Carreno-Luengo, H. (2014). Analysis of spaceborne GNSS-R delay-Doppler tracking. *IEEE Journal of Selected Topics in Applied Earth Observations and Remote Sensing*, *7*(5), 1481-1492.

Paziewski, J., and Crespi, M. (2020). High-precision multi-constellation GNSS: methods, selected applications and challenges. *Meas. Sci. Technol*, *31*(010101), 3pp.

Pell, O., Atasu, K., and Mencer, O. (2006, January). Accelerating Scientific Computations using FPGAs. The Advanced Maui Optical and Space Surveillance Technologies Conference, E97.

Rodriguez-Alvarez, N., Camps, A., Vall-Llossera, M., Bosch-Lluis, X., Monerris, A., Ramos-Perez, I., ... and Sanchez, N. (2010). Land geophysical parameters retrieval using the interference pattern GNSS-R technique. *IEEE Transactions on Geoscience and Remote Sensing*, *49*(1), 71-84.

Schonhoff, T. A., and Giordano, A. A. (2006). *Detection and estimation theory and its applications*. Prentice Hall.

Spilker Jr, J. J., and Van Dierendonck, A. J. (2001). Proposed new L5 civil GPS codes. *Navigation*, *48*(3), 135-143.

Spirent SIMGEN. (2022). SPIRENT SIMGEN Multi-GNSS Simulator Software Suite Datasheet and Specification. https://www.spirent.com/assets/u/datasheet-simgen Accessed (2022)

Spirent. (2022). SPIRENT GSS9000 GNSS Simulator Datasheet and Specification. https://www.spirent.com/assets/u/datasheet-gss9000-series Accessed (2022)

Tan, L., and Jiang, J. (2018). *Digital signal processing: fundamentals and applications*. Academic Press.

Tcherniakovski, D., Antonov, I., Kolotkin, A., and Kavaleuski, A. (2016, September). 4-channel Multiband All GNSS compliant RF Front End IC: Bringing Professional Level Equipment to Mass Market. In *Proceedings of the 29th International Technical Meeting of the Satellite Division of The Institute of Navigation (ION GNSS+ 2016)* pp. 459-469.

Troglia Gamba, M., Marucco, G., Pini, M., Ugazio, S., Falletti, E., and Lo Presti, L. (2015). Prototyping a GNSS-based passive radar for UAVs: An instrument to classify the water content feature of lands. *Sensors*, *15*(11), 28287-28313.

Tsai, Y. F., Yeh, W. H., Juang, J. C., Yang, D. S., and Lin, C. T. (2021). From GPS receiver to GNSS reflectometry payload development for the triton satellite mission. *Remote Sensing*, *13*(5), 999.

Tsui, J. B. Y. (2005). *Fundamentals of global positioning system receivers: a software approach*. John Wiley and Sons.

UltraScale, Z. (2017). Device Technical Reference Manual. *Xilinx*, *1*, 13-17.

Unwin, M., Jales, P., Blunt, P., Duncan, S., Brummitt, M., and Ruf, C. (2013, March). The SGR-ReSI and its application for GNSS reflectometry on the NASA EV-2 CYGNSS mission. In *2013 IEEE Aerospace Conference* (pp. 1-6). IEEE.

Varma, B. S. C., Paul, K., and Balakrishnan, M. (2013, January). Accelerating 3D-FFT using hard embedded blocks in FPGAs. In *2013 26th International Conference on VLSI Design and 2013 12th International Conference on Embedded Systems* (pp. 92-97). IEEE.

Vaughan, R. G., Scott, N. L., and White, D. R. (1991). The theory of bandpass sampling. *IEEE Transactions on signal processing*, *39*(9), 1973-1984.

Wu, S., T. Meehan, and L. Young (1997), The potential use of GPS signals as ocean altimetry observable*, in Proceedings of the 1997 National Technical Meeting of The Institute of Navigation*, pp. 543–550, Institute of Navigation (ION), Santa Monica, Calif.

Yan, Q., and Huang, W. (2016). Spaceborne GNSS-R sea ice detection using delay-Doppler maps: First results from the UK TechDemoSat-1 mission. *IEEE journal of selected topics in applied earth observations and remote sensing*, *9*(10), 4795-4801.

Zhang, Y., Wang, M., and Li, Y. (2018). Low computational signal acquisition for GNSS receivers using a resampling strategy and variable circular correlation time. *Sensors*, *18*(2), 678.

Zhuang, W., and Tranquilla, J. (1993). Digital baseband processor for the GPS receiver (parts I and II). *IEEE Transactions on Aerospace and Electronic Systems*, *29*(4), 1343-1349.

Zribi, M., Motte, E., Baghdadi, N., Baup, F., Dayau, S., Fanise, P., ... and Wigneron, J. P. (2018). Potential applications of GNSS-R observations over agricultural areas: Results from the GLORI airborne campaign. *Remote Sensing*, *10*(8), 1245.

Xilinx (2021) ZCU104 Evaluation Board for the Zynq UltraScale+ MPSoC. www.xilinx.com/products/boards-and-kits/zcu104.html. Accessed (2021)

Männel, B., Zus, F., Dick, G., Glaser, S., Semmling, M., Balidakis, K., ... & Schuh, H. (2021). GNSS-based water vapor estimation and validation during the MOSAiC expedition. Atmospheric Measurement Techniques, 14(7), 5127-5138.

Antonoglou, N., Balidakis, K., Wickert, J., Dick, G., de la Torre, A., & Bookhagen, B. (2022). Water-Vapour Monitoring from Ground-Based GNSS Observations in Northwestern Argentina. Remote Sensing, 14(21), 5427.